remote sensing

MDPI

Article

A Fast Atmospheric Trace Gas Retrieval for Hyperspectral Instruments Approximating Multiple Scattering—Part 1: Radiative Transfer and a Potential OCO-2 XCO_2 Retrieval Setup

Maximilian Reuter *, Michael Buchwitz, Oliver Schneising, Stefan Noël, Vladimir Rozanov, Heinrich Bovensmann and John P. Burrows

Institute of Environmental Physics, University of Bremen, P.O. Box 330440, 28334 Bremen, Germany; Michael.Buchwitz@iup.physik.uni-bremen.de (M.B.); schneising@iup.physik.uni-bremen.de (O.S.); Stefan.Noel@iup.physik.uni-bremen.de (S.N.); rozanov@iup.physik.uni-bremen.de (V.R.); heinrich.bovensmann@iup.physik.uni-bremen.de (H.B.); burrows@iup.physik.uni-bremen.de (J.P.B.)
* Correspondence: mail@maxreuter.org

Received: 31 August 2017; Accepted: 7 November 2017; Published: 11 November 2017

Abstract: Satellite retrievals of the atmospheric dry-air column-average mole fraction of CO_2 (XCO_2) based on hyperspectral measurements in appropriate near (NIR) and short wave infrared (SWIR) O_2 and CO_2 absorption bands can help to answer important questions about the carbon cycle but the precision and accuracy requirements for XCO_2 data products are demanding. Multiple scattering of light at aerosols and clouds can be a significant error source for XCO_2 retrievals. Therefore, so called full physics retrieval algorithms were developed aiming to minimize scattering related errors by explicitly fitting scattering related properties such as cloud water/ice content, aerosol optical thickness, cloud height, etc. However, the computational costs for multiple scattering radiative transfer (RT) calculations can be immense. Processing all data of the Orbiting Carbon Observatory-2 (OCO-2) can require up to thousands of CPU cores and the next generation of CO_2 monitoring satellites will produce at least an order of magnitude more data. Here we introduce the Fast atmOspheric traCe gAs retrievaL FOCAL including a scalar RT model which approximates multiple scattering effects with an analytic solution of the RT problem of an isotropic scattering layer and a Lambertian surface. The computational performance is similar to an absorption only model and currently determined by the convolution of the simulated spectra with the instrumental line shape function (ILS). We assess FOCAL's quality by confronting it with accurate multiple scattering vector RT simulations using SCIATRAN. The simulated scenarios do not cover all possible geophysical conditions but represent, among others, some typical cloud and aerosol scattering scenarios with optical thicknesses of up to 0.7 which have the potential to survive the pre-processing of a XCO_2 algorithm for real OCO-2 measurements. Systematic errors of XCO_2 range from -2.5 ppm (-6.3‰) to 3.0 ppm (7.6‰) and are usually smaller than ± 0.3 ppm (0.8‰). The stochastic uncertainty of XCO_2 is typically about 1.0 ppm (2.5‰). FOCAL simultaneously retrieves the dry-air column-average mole fraction of H_2O (XH_2O) and the solar induced chlorophyll fluorescence at 760 nm (SIF). Systematic and stochastic errors of XH_2O are most times smaller than ± 6 ppm and 9 ppm, respectively. The systematic SIF errors are always below 0.02 $mW/m^2/sr/nm$, i.e., it can be expected that instrumental or forward model effects causing an in-filling of the used Fraunhofer lines will dominate the systematic errors when analyzing actually measured data. The stochastic uncertainty of SIF is usually below 0.3 $mW/m^2/sr/nm$. Without understating the importance of analyzing synthetic measurements as presented here, the actual retrieval performance can only be assessed by analyzing measured data which is subject to part 2 of this publication.

Keywords: CO_2; satellite remote sensing; OCO-2; radiative transfer

1. Introduction

Satellite retrievals of the atmospheric dry-air column-average mole fraction of CO_2 (XCO_2) based on hyperspectral measurements in appropriate near (NIR) and short wave infrared (SWIR) O_2 and CO_2 absorption bands can help to answer pressing questions about the carbon cycle [1]. However, the precision and even more the accuracy requirements for applications like surface flux inversion or emission monitoring are demanding [2–4]. As an example, large scale biases of a few tenths of a ppm can already hamper an inversion with mass-conserving global inversion models [2,3].

Several theoretical studies suggest that multiple scattering at aerosols and clouds are a significant error source for XCO_2 retrievals [5–7]. Therefore, so called full physics retrievals were set up aiming to minimize these scattering related errors by explicitly fitting scattering related properties such as cloud water/ice content, aerosol optical thickness, cloud height, etc. [8–12].

However, due to limited information content in the used absorption bands [13–15], only few scattering parameters can simultaneously be retrieved, i.e., many other properties (e.g., scattering phase function (SPF), number of cloud layers, etc.) rely on empirical estimates. Additionally, the needed RT calculations with multiple scattering (especially with polarization) can produce computational costs which are several orders of magnitude larger than for absorption only models. This is true even when making use of short cuts and approximations such as the low streams interpolation method [12], correlated-k method [16], or neglecting RT effects like polarization [17]. Much larger speedups can be achieved by, e.g., tabulating the RT [18] or with the photon path-length distribution function (PPDF) method [19,20].

A recent study comparing OCO-2 Orbiting Carbon Observatory-2 [21,22] and GOSAT Greenhouse Gases Observing Satellite [23] XCO_2 retrievals with and without any explicit consideration of scattering at clouds and aerosols suggests that the introduced errors in measured data are small after appropriate filtering [24]. Additionally, Bril et al. showed with simulated and measured GOSAT data that considering scattering at only one layer can be sufficient to obtain results with state of the art precision and accuracy [20].

Within the next section, we propose a scalar RT model which approximates multiple scattering effects at an optically thin isotropic scattering layer with only little extra computational costs compared to an absorption only RT model. This model is the heart of the Fast atmOspheric traCe gAs retrievaL FOCAL which is introduced in Section 3. In this section, we also introduce various FOCAL setups and perform retrieval experiments for an OCO-2 like instrument. These experiments are not aiming to comprehensively cover the majority of potential geophysical scenarios, because the final quality depends on the full retrieval scheme including, e.g., potential instrument and forward model errors and different post-filtering capabilities. The aim is rather to identify a promising candidate retrieval setup serving as starting point for the development of a full retrieval scheme and its application to actually measured OCO-2 data. Whilst part 1 of this publication is on theoretical aspects of the RT and the retrieval, part 2 [25] deals with the application to measured OCO-2 data including noise model, zero level offset, pre- and post-filtering, bias correction, and validation.

2. Radiative Transfer

Let, for now, the model atmosphere consist of a plane parallel, vertically heterogeneous, absorbing atmosphere, a surface with Lambertian reflectance, and an optically thin scattering layer of infinitesimal geometrical thickness (Figure 1). Light hitting the scattering layer may either be transmitted without interaction, absorbed, or isotropically scattered into the upper or lower hemisphere (or half-space). In the following, we derive an equation for the satellite measured radiance I for a plane parallel geometry; in Section 2.11, we adapt our results for a pseudo spherical geometry.

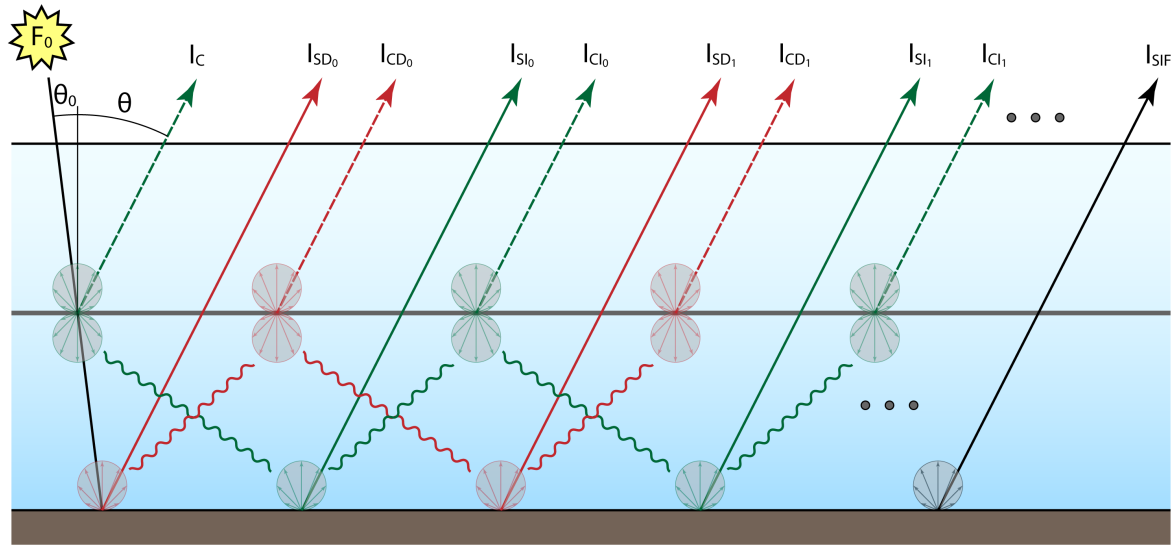

Figure 1. Basic radiative transfer setup with an absorbing atmosphere, a surface with Lambertian reflectance, and an optically thin semi-transparent layer which can partly transmit, absorb, or scatter light in an isotropic way. F_0 is the solar incoming flux, θ_0 and θ are the solar and satellite zenith angles, and I is the radiance reaching the satellite instrument split into components as discussed in the main text. Red represents radiation originating from direct illumination of the surface. Green represents radiation originating from direct illumination of the scattering layer. Arrows represent radiance components reaching the satellite instrument originating from the surface (solid) or from the scattering layer (dashed). Waved lines represent diffuse radiant fluxes.

We separate the radiance reaching the satellite instrument in the components I_C, I_{SD}, I_{CD}, I_{SI}, I_{CI}, and I_{SIF}:

$$I = I_C + I_{SD} + I_{CD} + I_{SI} + I_{CI} + I_{SIF} \tag{1}$$

I_C is the radiance directly scattered from the scattering layer to the satellite. I_{SD} represents the radiance originating from the surface due to direct illumination of the surface and includes components due to multiple scattering of the Lambertian surface flux (I_{SD_i}). I_{CD} represents the radiance originating from the scattering layer due to direct illumination of the surface including components due to multiple scattering (I_{CD_i}). I_{SI} represents the radiance originating from the surface due to diffuse illumination of the surface including components due to multiple scattering (I_{SI_i}). I_{CI} represents the radiance originating from the scattering layer due to diffuse illumination of the surface including components due to multiple scattering (I_{CI_i}). I_{SIF} is the radiance originating from solar induced chlorophyll fluorescence at 760 nm (SIF) transmitted through the scattering layer but ignoring multiple scattering because of the weak signal.

If not otherwise noted, in the following, F stands for flux, I for intensity (radiance), T for transmittance, τ for vertical optical thickness, and g for gaseous absorption. A superscript s stands for the scattering layer in general. A subscript e, a, and s stand for extinction, absorption, and scattering of the scattering layer, respectively. As an example, the term T_I^g represents a transmittance of intensity through a gaseous absorber.

2.1. Radiance Transmission

The transmittance T_I^g along a slant light path through a plane parallel atmospheric layer with gaseous absorption can be computed with Beer-Lambert's law

$$\begin{aligned} T_I^g(\tau_g, \zeta) &= e^{-\zeta \int K(z)\, dz} \\ &= e^{-\zeta\, \tau_g} \end{aligned} \tag{2}$$

with K being the absorption coefficient, z the height above the surface, τ_g the total vertical optical thickness, and $\zeta = 1/\cos\theta$ the light path extension for the zenith angle θ.

Considering light scattering and absorption within the scattering layer, the fraction of light transmitted through the scattering layer becomes

$$T_I^s(\tau_e, \zeta) = e^{-\tau_e \zeta} = 1 - S_I(\tau_s, \tau_e, \zeta) - A_I(\tau_s, \tau_e, \zeta); \tag{3}$$

with $\tau_e = \tau_a + \tau_s$ being the extinction optical thickness, i.e., the sum of absorption (not to be confused with gaseous absorption) and scattering optical thickness. S_I and A_I are the fraction of scattered and absorbed radiance within the scattering layer:

$$S_I(\tau_s, \tau_e, \zeta) = \frac{\tau_s}{\tau_e} \left[1 - T_I^s(\tau_e, \zeta)\right] \tag{4}$$

$$A_I(\tau_s, \tau_e, \zeta) = \frac{\tau_a}{\tau_e} \left[1 - T_I^s(\tau_e, \zeta)\right] \tag{5}$$

2.2. Irradiance Transmission

The transmittance of the radiant flux originating from a Lambertian source through a plane parallel atmospheric layer can be computed by integrating over the hemisphere (see, e.g., the textbook of Roedel [26]):

$$T_F^g(\tau_g) = \frac{1}{\pi} \int_0^{2\,\pi} \int_0^{\frac{\pi}{2}} e^{-\frac{\tau_g}{\cos\theta}} \cos\theta \sin\theta \, d\theta \, d\varphi. \tag{6}$$

Integration over the azimuth angle φ and substituting $\zeta = 1/\cos\theta$ gives

$$T_F^g(\tau_g) = 2 \int_1^{\infty} \frac{e^{-\tau_g \zeta}}{\zeta^3} \, d\zeta, \tag{7}$$

which is basically the definition of the third exponential integral E_3

$$T_F^g(\tau_g) = 2\, E_3(\tau_g). \tag{8}$$

Analogously, the flux transmitted through the atmosphere below the scattering layer (with gaseous optical thickness $\tau_\downarrow$) plus the scattering layer becomes

$$T_F^{gs}(\tau_\downarrow + \tau_e) = 2\, E_3(\tau_\downarrow + \tau_e). \tag{9}$$

So that the relative additional extinction due to the scattering layer becomes

$$E_F(\tau_e, \tau_\downarrow) = 1 - \frac{E_3(\tau_\downarrow + \tau_e)}{E_3(\tau_\downarrow)}. \tag{10}$$

This can be separated into a fraction of scattered and absorbed flux within the scattering layer:

$$S_F(\tau_s, \tau_e, \tau_\downarrow) = \frac{\tau_s}{\tau_e} E_F(\tau_e, \tau_\downarrow) \tag{11}$$

$$A_F(\tau_s, \tau_e, \tau_\downarrow) = \frac{\tau_a}{\tau_e} E_F(\tau_e, \tau_\downarrow) \tag{12}$$

Note that Equation (7) could also be interpreted as theorem of equivalence in the form used by Bennartz and Preusker [27] but accounting only for photon path extensions and a PPDF specific for an isotropic scattering layer.

2.3. Solar Radiation

The solar incoming flux shall be F_0. As only Lambertian surfaces are considered in our model, the radiance components I_C, I_{SD}, I_{CD}, I_{SI}, and I_{CI} become proportional to

$$I_0 = \frac{F_0}{\pi \zeta_0} \; T_I^g(\tau_\uparrow, \zeta_0 + \zeta). \tag{13}$$

Here $\tau_\uparrow$ is the gaseous optical thickness above the scattering layer and ζ_0 or ζ the light path extension for the solar or satellite zenith angle θ_0 or θ. $T_I^g(\tau_\uparrow, \zeta_0 + \zeta)$ corresponds to the transmission along the slant light path from the sun to the scattering layer and from the scattering layer to the satellite.

2.4. I_C

I_C is the radiance directly scattered from the scattering layer to the satellite

$$I_C = I_0 \; S_I(\tau_s, \tau_e, \zeta_0) \; b, \tag{14}$$

where b corresponds to the fraction of radiation scattered into the hemisphere in backward direction, i.e., the upper or lower hemisphere for light coming from the sun or the surface. Analogously, f is the fraction of radiation scattered into the hemisphere in forward direction and

$$1 = f + b. \tag{15}$$

2.5. I_{SD}

I_{SD} represents the radiance originating from the surface due to direct illumination of the surface and includes components due to multiple scattering of the Lambertian surface flux (I_{SD_i}). This means, solar radiation transmits directly through the scattering layer ($T_I^s(\tau_e, \zeta_0)$) and the atmosphere below ($T_I^g(\tau_\downarrow, \zeta_0)$) and illuminates the surface with an Lambertian albedo α. This produces an upward flux which is in parts transmitted, absorbed, and scattered into the upper hemisphere, or back scattered into the lower hemisphere when reaching the scattering layer. The back scattered part contributes to the illumination of the surface and so on. The radiance component I_{SD_i} corresponds to the directly transmitted radiance from the surface through the lower atmosphere ($T_I^g(\tau_\downarrow, \zeta)$), the scattering layer ($T_I^s(\tau_e, \zeta)$), and the upper atmosphere after i-times of diffuse reflection between surface and scattering layer ($\alpha \; S_F(\tau_s, \tau_e, \tau_\downarrow) \; b \; [T_F^g(\tau_\downarrow)]^2$). Summing up all individual radiance components I_{SD_i} results in the following geometric series:

$$\begin{aligned} I_{SD} &= I_0 \; \alpha \; T_I^s(\tau_e, \zeta_0) \; T_I^s(\tau_e, \zeta) \; T_I^g(\tau_\downarrow, \zeta_0) \; T_I^g(\tau_\downarrow, \zeta) \; \sum_{i=0}^{\infty} \left(\alpha \; S_F(\tau_s, \tau_e, \tau_\downarrow) \; b \; \left[T_F^g(\tau_\downarrow) \right]^2 \right)^i & (16) \\ &= I_0 \; \alpha \; T_I^s(\tau_e, \zeta_0) \; T_I^s(\tau_e, \zeta) \; T_I^g(\tau_\downarrow, \zeta_0) \; T_I^g(\tau_\downarrow, \zeta) \; \frac{1}{1 - \alpha \; S_F(\tau_s, \tau_e, \tau_\downarrow) \; b \; \left[T_F^g(\tau_\downarrow) \right]^2} & (17) \end{aligned}$$

2.6. I_{CD}

I_{CD} represents the radiance originating from the scattering layer due to direct illumination of the surface and includes components due to multiple scattering of the Lambertian surface flux (I_{CD_i}). As for I_{SD}, solar radiation transmits directly through the scattering layer ($T_I^s(\tau_e, \zeta_0)$) and the atmosphere below ($T_I^g(\tau_\downarrow, \zeta_0)$) and illuminates the surface with an Lambertian albedo α. This produces an upward flux which is in parts transmitted, absorbed, and scattered into the upper hemisphere, or back scattered into the lower hemisphere when reaching the scattering layer. The back scattered part contributes to the illumination of the surface and so on. The radiance component I_{CD_i} originates from the scattering layer due to the diffuse surface flux transmitting the lower atmosphere ($T_F^g(\tau_\downarrow)$) and getting scattered

into the upper hemisphere ($f\ S_F(\tau_s, \tau_e, \tau_\downarrow)$) after i-times of diffuse reflection between surface and scattering layer ($\alpha\ S_F(\tau_s, \tau_e, \tau_\downarrow)\ b\ [T_F^g(\tau_\downarrow)]^2$). Summing up all individual radiance components I_{CD_i} results in the following geometric series:

$$I_{CD} = I_0\ \alpha\ T_I^s(\tau_e, \zeta_0)\ S_F(\tau_s, \tau_e, \tau_\downarrow)\ f\ T_I^g(\tau_\downarrow, \zeta_0)\ T_F^g(\tau_\downarrow)\ \frac{1}{1 - \alpha\ S_F(\tau_s, \tau_e, \tau_\downarrow)\ b\ \left[T_F^g(\tau_\downarrow)\right]^2} \quad (18)$$

2.7. I_{SI}

I_{SI} represents the radiance originating from the surface due to diffuse illumination of the surface by the scattering layer and includes components due to multiple scattering of the isotropic downward flux of the scattering layer (I_{SI_i}). Here we follow that part of the solar radiation which is diffusely scattered downward by the scattering layer ($f\ S_I(\tau_s, \tau_e, \zeta_0)$) and transmitted to the surface ($T_F^g(\tau_\downarrow)$). The illuminated surface produces an upward flux which is in parts transmitted, absorbed, and scattered into the upper hemisphere, or back scattered into the lower hemisphere when reaching the scattering layer. The back scattered part contributes to the diffuse illumination of the surface and so on. The radiance component I_{SI_i} corresponds to the directly transmitted radiance from the surface through the lower atmosphere ($T_I^g(\tau_\downarrow, \zeta)$), the scattering layer ($T_I^s(\tau_e, \zeta)$), and the upper atmosphere after i-times of diffuse reflection between surface and scattering layer ($\alpha\ S_F(\tau_s, \tau_e, \tau_\downarrow)\ b\ [T_F^g(\tau_\downarrow)]^2$). Summing up all individual radiance components I_{SI_i} results in the following geometric series:

$$I_{SI} = I_0\ \alpha\ S_I(\tau_s, \tau_e, \zeta_0)\ f\ T_I^s(\tau_e, \zeta)\ T_F^g(\tau_\downarrow)\ T_I^g(\tau_\downarrow, \zeta)\ \frac{1}{1 - \alpha\ S_F(\tau_s, \tau_e, \tau_\downarrow)\ b\ \left[T_F^g(\tau_\downarrow)\right]^2} \quad (19)$$

2.8. I_{CI}

I_{CI} represents the radiance originating from the scattering layer due to diffuse illumination of the scattering layer and includes components due to multiple scattering of the isotropic downward flux of the scattering layer (I_{CI_i}). Again we follow that part of the solar radiation which is diffusely scattered downward by the scattering layer ($f\ S_I(\tau_s, \tau_e, \zeta_0)$) and transmitted to the surface ($T_F^g(\tau_\downarrow)$). The illuminated surface produces an upward flux which is in parts transmitted, absorbed, and scattered into the upper hemisphere, or back scattered into the lower hemisphere when reaching the scattering layer. The back scattered part contributes to the diffuse illumination of the surface and so on. The radiance component I_{CI_i} originates from the scattering layer due to the diffuse surface flux transmitting the lower atmosphere ($T_F^g(\tau_\downarrow)$) and getting scattered into the upper hemisphere ($f\ S_F(\tau_s, \tau_e, \tau_\downarrow)$) after i-times of diffuse reflection between surface and scattering layer ($\alpha\ S_F(\tau_s, \tau_e, \tau_\downarrow)\ b\ [T_F^g(\tau_\downarrow)]^2$). Summing up all individual radiance components I_{CI_i} results in the following geometric series:

$$I_{CI} = I_0\ \alpha\ S_I(\tau_s, \tau_e, \zeta_0)\ S_F(\tau_s, \tau_e, \tau_\downarrow)\ f^2\ \left[T_F^g(\tau_\downarrow)\right]^2\ \frac{1}{1 - \alpha\ S_F(\tau_s, \tau_e, \tau_\downarrow)\ b\ \left[T_F^g(\tau_\downarrow)\right]^2} \quad (20)$$

2.9. I_{SIF}

I_{SIF} is the radiance originating from the isotropic solar induced chlorophyll fluorescence flux F_{SIF}^0 at the surface transmitted through the atmosphere ($T_I^g(\tau_\downarrow + \tau_\uparrow, \zeta)$) and the scattering layer ($T_I^s(\tau_e, \zeta)$) but ignoring multiple scattering because of the weak signal.

$$I_{SIF} = \frac{F_{SIF}^0}{\pi}\ T_I^s(\tau_e, \zeta)\ T_I^g(\tau_\downarrow + \tau_\uparrow, \zeta) \quad (21)$$

2.10. Approximations

By means of the following approximations, we are reducing the complexity of the final result which further enhances the computational efficiency. Note that this also considerably reduces the complexity of the (analytic) partial derivatives needed to compute the Jacobian (used by the retrieval).

Due to the high accuracy requirements for the retrieval of greenhouse gases, we are primarily interested in scenarios where scattering at aerosols and clouds is minimal, even if the retrieval algorithm is, in principle, capable of reducing scattering related errors.

Additionally, we are primarily interested in accurate greenhouse gas concentrations; inaccuracies in the retrieved scattering properties are less important. For these reasons, we make an approximation for small extinction optical thicknesses.

Further, we assume that the spectral signal produced by absorption within the scattering layer cannot easily be disentangled from an albedo and scattering signal. For some cases, it is even identical; e.g., when the single scattering albedo ($\omega = \tau_s/\tau_e$) becomes zero, the absorption and the albedo signal become identical. Therefore, we are not aiming to explicitly retrieve the absorption within the scattering layer and approximate that $\tau_a = 0$ (i.e., $\tau_e = \tau_s$). As a result, the retrieved albedo and the amount of scattered radiation may be slightly off, which does not pose a problem as long as the retrieved greenhouse gas concentrations are not affected.

Additionally, we assume that the light is scattered in same parts into the upper and lower hemisphere at the scattering layer ($f = b = 1/2$), which is reasonable especially for an optically thin scattering layer.

First order Taylor series approximation of Equations (4) and (3) gives

$$S_I(\tau_s, \zeta) \approx \zeta\ \tau_s \text{ and} \tag{22}$$

$$T_I^s(\tau_s, \zeta) \approx 1 - S_I(\tau_s, \zeta). \tag{23}$$

The amount of diffuse scattered radiant flux (Equation (11)) simplifies to

$$S_F(\tau_s, \tau_\downarrow) \approx \frac{E_2(\tau_\downarrow)}{E_3(\tau_\downarrow)}\ \tau_s. \tag{24}$$

Here E_2 is the second exponential integral and $E_2(\tau_\downarrow)/E_3(\tau_\downarrow)$ a number always between 1 and 2.

Substituting Equations (22)–(24) into Equations (17)–(21) and subsequently first order Taylor series approximation of Equation (1) at $\tau_s = 0$ as done in Appendix A yields:

$$\begin{aligned} I \approx\ & \tfrac{F_0}{\pi\zeta_0}\ T_I^g(\tau_\uparrow, \zeta_0 + \zeta)\ \left[\tfrac{1}{2}\ \zeta_0\ \tau_s + \right. \\ & \alpha\ \left(T_I^g(\tau_\downarrow, \zeta_0 + \zeta)\ \left[1 - (\zeta_0 + \zeta)\ \tau_s + 2\,\alpha\ E_2(\tau_\downarrow)\ E_3(\tau_\downarrow)\ \tau_s\right] + \right. \\ & \left.\left. T_I^g(\tau_\downarrow, \zeta_0)\ E_2(\tau_\downarrow)\ \tau_s + \ T_I^g(\tau_\downarrow, \zeta)\ E_3(\tau_\downarrow)\ \zeta_0\ \tau_s\right)\right] + \\ & \tfrac{F_{SIF}^0}{\pi}\ T_I^g(\tau_\downarrow + \tau_\uparrow, \zeta)\ \left[1 - \zeta\ \tau_s\right]. \end{aligned} \tag{25}$$

2.11. Pseudo-Spherical Geometry

Due to the spherical geometry of the Earth's atmosphere (Figure 2), the (solar and satellite) zenith angle changes with height z.

$$\theta(z) = \arcsin\left(\frac{r_e}{r_e + z}\ \sin\theta\right), \tag{26}$$

with r_e being the Earth's radius and θ the (solar or satellite) zenith angle at the surface.

Correspondingly, also the light path extensions ζ and ζ_0 become height dependent. In the following, θ, θ_0, ζ, and ζ_0 shall refer to values defined at the surface. $\theta(z)$, $\theta_0(z)$, $\zeta(z)$, and $\zeta_0(z)$

shall refer to height z (Equation (26)) and θ^s, θ^s_0, ζ^s, and ζ^s_0 shall refer to the scattering layer. This has implications for Equation (2) which now becomes

$$T^g_I(K(z), \zeta(z)) = e^{-\int K(z)\ \zeta(z)\ dz}. \tag{27}$$

Additionally, ζ in Equations (3), (4), (5), (22) and (24) has to be replaced with the corresponding value at the scattering layer ζ^s.

In order to keep the integral in Equation (6) simple, we do not account for the spherical geometry for the transmission of the diffuse fluxes contributing to multiple scattering. For this reason, we consider this approach a pseudo-spherical approximation.

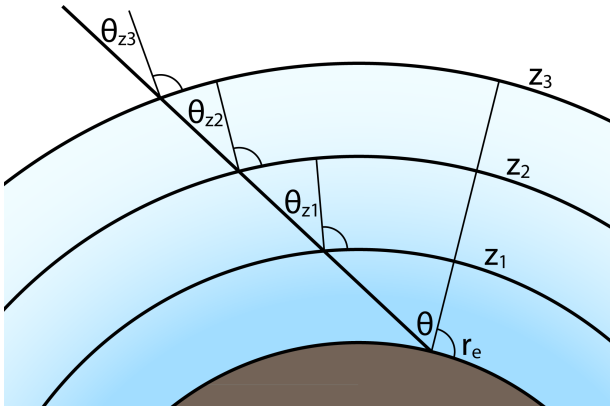

Figure 2. Spherical geometry of the Earth's atmosphere with the Earth's radius r_e, the (solar or satellite) zenith angle θ at the surface and at the heights $z_{1,2,3}$.

3. Retrieval

The retrieval presented in this section may be applied to various passive hyperspectral satellite instruments operating in the NIR or SWIR and may be used to gain information on various gaseous species with suitable absorption bands. However, here we concentrate on the retrieval of XCO_2 (plus XH_2O and SIF) from an OCO-2 like satellite instrument.

OCO-2 was launched in July 2014 and is part of the A-train satellite constellation. It flies in a sun-synchronous orbit crossing the equator at 13:36 local time. OCO-2 measures one linear polarization direction of the solar backscattered radiance in three independent wavelength bands: the O_2-A band at around 760 nm (band 1) with a spectral resolution of about 0.042 nm and a spectral sampling of about 0.015 nm, the weak CO_2 band at around 1610 nm (band 2) with a spectral resolution of about 0.080 nm and a spectral sampling of about 0.031 nm, and the strong CO_2 band at around 2060 nm (band 3) with a spectral resolution of about 0.103 nm and a spectral sampling of about 0.040 nm. OCO-2 is operated in a near-push-broom fashion and has eight footprints across track and an integration time of 0.333 s. The instrument's spatial resolution at ground is 1.29 km across track and 2.25 km along track. More information on the OCO-2 instrument can be obtained from the publications of Crisp et al. [21,22].

3.1. Setup

The aim of the retrieval is to find the most probable atmospheric state (especially the CO_2 concentration) given an OCO-2 measurement and some a priori knowledge. According to the textbook of Rodgers [28] and as done by, e.g., Reuter et al. [17], this can be achieved by minimizing the cost function

$$\begin{aligned} \chi^2 \quad = \quad & \frac{1}{m+n} \left[(\vec{y} - \vec{F}(\vec{x}, \vec{b}))^T \, \mathbf{S}_\epsilon^{-1} \, (\vec{y} - \vec{F}(\vec{x}, \vec{b})) \right. \\ & \left. + (\vec{x} - \vec{x}_a)^T \, \mathbf{S}_a^{-1} \, (\vec{x} - \vec{x}_a) \right]. \end{aligned} \tag{28}$$

iteratively with the Gauss-Newton method until convergence is reached.

$$\vec{x}_{i+1} = \vec{x}_i + \hat{\mathbf{S}}_i \left[\mathbf{K}_i^T \mathbf{S}_\epsilon^{-1} \left(\vec{y} - \vec{F}(\vec{x}_i, \vec{b})\right) - \mathbf{S}_a^{-1} \left(\vec{x}_i - \vec{x}_a\right)\right] \quad (29)$$

$$\hat{\mathbf{S}}_i = \left(\mathbf{K}_i^T \mathbf{S}_\epsilon^{-1} \mathbf{K}_i + \mathbf{S}_a^{-1}\right)^{-1} \quad (30)$$

All quantities used in these equations are explained and discussed in the following.

3.1.1. Measurement Vector y

The measurement vector contains that data measured by the instrument from which we want to gain knowledge about the atmosphere (e.g., the CO_2 concentration). Each of OCO-2's bands consists of 1016 spectral pixels which we group into four fit windows: SIF (∼758.26–759.24 nm), O_2 (∼757.65–772.56 nm), wCO_2 (∼1595.0–1620.6 nm), and sCO_2 (∼2047.3–2080.9 nm). The center wavelengths of the individual spectral pixels have been obtained from an example OCO-2 L1b file (oco2_L1bScGL_04243a_150419_B7000r_150608142047.h5, *https://daac.gsfc.nasa.gov*). The separate SIF fit window ensures that the SIF information solely comes from free Fraunhofer lines rather than from O_2 absorption features which makes it much easier to avoid misinterpretations with scattering properties [29]. The measurement vector is of dimension $m \times 1$ ($m \approx 2600$) and an example is illustrated in Figure 3 (top). Note that within this publication, the measurement vector consists of simulated observations for which the true atmospheric state is known.

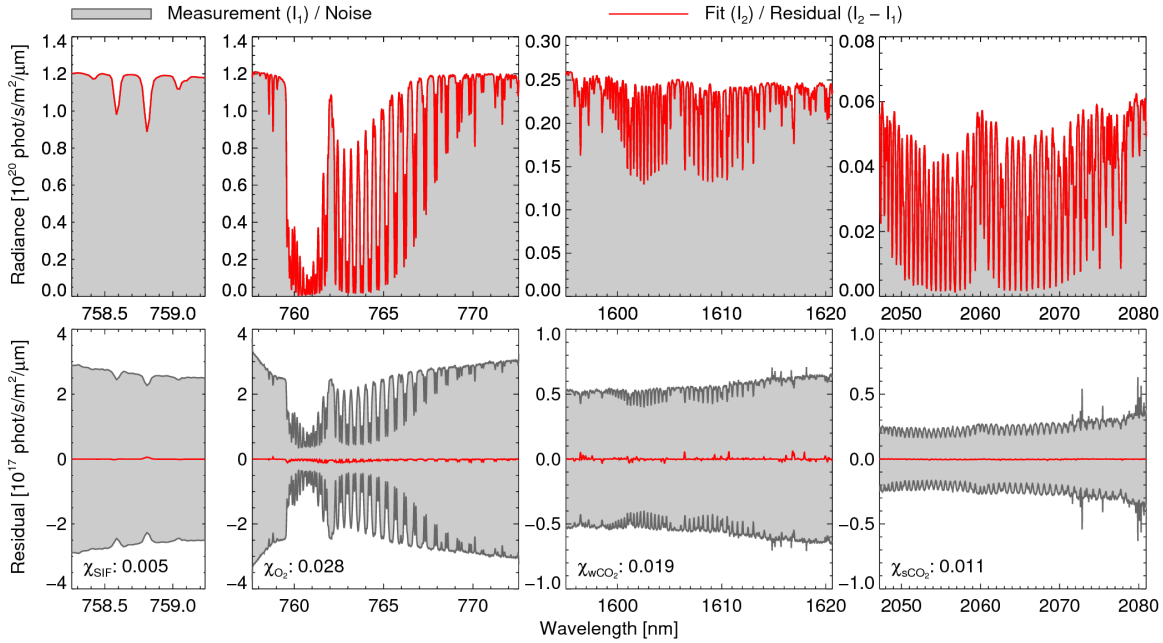

Figure 3. SCIATRAN simulated OCO-2 measurement fitted with FOCAL. Geophysical *baseline* scenario and *0-Scat* retrieval setup, $\theta_0 = 40°$, parallel polarization. See Section 3.2 for definitions of geophysical scenarios and retrieval setups. **Top**: Simulated and fitted radiance measurement in gray and red, respectively. **Bottom**: Simulated measurement noise and fit residual $\vec{\Delta y} = \vec{I}_2 - \vec{I}_1$ (fit minus measurement) in gray and red, respectively. An estimate of the goodness of fit (relative to the noise) in fit window j is computed by $\chi_j = (\frac{1}{m_j} \vec{\Delta y}_j^T \mathbf{S}_{\epsilon_j}^{-1} \vec{\Delta y}_j)^{1/2}$.

3.1.2. Measurement Error Covariance Matrix $\mathbf{S}_\epsilon$

Strictly speaking, the measurement error covariance matrix does not only quantify the measurement errors and their correlations; it, additionally, accounts for the forward model error. However, for this study, we assume the measurement error to dominate and that no cross correlations

exist, i.e., $\mathbf{S}_\epsilon$ becomes diagonal. We use the noise parameterization as provided by the same OCO-2 L1b example file mentioned above to compute the diagonal elements of $\mathbf{S}_\epsilon$. The measurement error covariance matrix is of dimension $m \times m$ and an example is illustrated in Figure 3 (bottom).

3.1.3. Forward Model $\vec{F}$

The forward model is a vector function of dimension $m \times 1$ that simulates the measurement vector, i.e., OCO-2 measurements. Its inputs are the state and parameter vector defining the geophysical and instrumental state. Primarily, the forward model consists of the RT model described in Section 2. The RT computations require a discretization of the atmosphere which we split into 20 homogeneous layers, each containing the same number of dry-air particles (i.e., molecules).

Additionally to the RT calculations, the forward model simulates the instrument by convolving the RT simulations performed on a fixed high resolution wavelength grid with the instrumental line shape function (ILS) obtained from the same OCO-2 L1b example file mentioned above. Furthermore, the forward model has the ability to simulate zero level offsets (i.e., additive radiance offsets), shift and squeeze the wavelength axes of the fit windows according to Equation (31), and squeeze the ILS according to Equation (33).

$$\lambda' = \lambda + \lambda_{\text{sh}} + \lambda_n \, \lambda_{\text{sq}} \tag{31}$$

$$\lambda_n = 2 - 4 \, \frac{\lambda_1 - \lambda}{\lambda_1 - \lambda_0} \tag{32}$$

Here λ' is the modified wavelength, λ the nominal wavelength, λ_{sh} the wavelength shift parameter, λ_n the normalized nominal wavelength, λ_{sq} the wavelength squeeze parameter, and $\lambda_{0,1}$ the minimum or maximum of λ, respectively. The normalization of λ is done in a way that the average absolute value of λ_n is approximately one.

$$\lambda'_{\text{ILS}} = \lambda_{\text{ILS}} \, \text{ILS}_{\text{sq}} \tag{33}$$

Here λ'_{ILS} is the modified ILS wavelength computed from the nominal ILS λ_{ILS} wavelength and the squeeze parameter ILS_{sq}.

3.1.4. State Vector $\vec{x}$

The state vector consists of all quantities which we retrieve from the measurement and is of dimension $n \times 1$ with $n = 36$. The dry-air mole fractions of water vapor (H_2O) and CO_2 are retrieved from both CO_2 fit windows within five layers splitting the atmosphere into parts containing the same number of dry-air particles. This means, each CO_2 and H_2O layer spans over four atmospheric layers used for the discretized RT calculations. The CO_2 and H_2O concentrations are homogeneous within each of the five layers. XCO_2 and XH_2O are not part of the state vector but are calculated during the post processing from the layer concentrations.

SIF at 760 nm is derived from the SIF fit window by scaling the SIF reference spectrum F^0_{SIF}. The scattering parameters pressure (i.e., height) of the scattering layer p_s (in units of the surface pressure p_0), scattering optical thickness at 760 nm τ_s, and Ångström exponent Å are derived from all fit windows simultaneously.

Within the SIF fit window, FOCAL additionally fits a first order polynomial of the spectral albedo $\alpha P_{0,1}$ and shift and squeeze of the wavelength axis $\lambda_{\text{sh,sq}}$. Within the other fit windows, FOCAL additionally fits a second order polynomial of the spectral albedo $\alpha P_{0,1,2}$, shift and squeeze of the wavelength axis, and a squeeze of the instrumental line shape function ILS_{sq}.

We estimate the first guess zeroth order albedo polynomial coefficients αP_0 from the continuum reflectivities $R_0 = \pi \, \zeta_0 \, I / F_0$ using up to nine spectral pixels at the fit windows' lower wavelength length ends. The first guess profiles of H_2O and CO_2 are obtained from ECMWF (European Centre for

Medium-Range Weather Forecasts) analysis fields and SECM2016, respectively. SECM2016 corresponds to the simple empirical carbon model described by Reuter et al. [30] but trained with version CT2016 of the CarbonTracker model [31]. All other first guess state vector elements are scene independent and the a priori state vector $\vec{x}_a$ equals the first guess state vector $\vec{x}_0$.

Table 1 summarizes the state vector composition including the used fit windows, a priori $\vec{x}_a$ and first guess $\vec{x}_0$ values, a priori uncertainties $\sigma\vec{x}_a$, and typical values of a posteriori uncertainties $\sigma\hat{\vec{x}}$ and the degrees of freedom for signal d_s.

Table 1. State vector composition of the baseline, i.e., the *3-Scat* retrieval setup (see Section 3.2.1 for definition of retrieval setups). From left to right, the columns represent the name of the state vector element, its sensitivity within the four fit windows, a priori $\vec{x}_a$ and first guess $\vec{x}_0$ value, the a priori uncertainty $\sigma\vec{x}_a$, the a posteriori uncertainty $\sigma\hat{\vec{x}}$, and the degrees of freedom d_s. A posteriori uncertainty and degrees of freedom represent results of the geophysical *Rayleigh* scenario, $\theta_0 = 40°$, and perpendicular polarization.

State Vector Element	Fit Window Sensitivity				$\vec{x}_a, \vec{x}_0$	$\sigma\vec{x}_a$	$\sigma\hat{\vec{x}}$	d_s
	SIF	O_2	wCO_2	sCO_2				
αP_0^{SIF}	•				R_0^{SIF}	0.1	0.0016	1.00
αP_1^{SIF}	•				0.0	0.01	0.0008	0.99
$\alpha P_0^{O_2}$		•			$R_0^{O_2}$	0.1	0.0000	1.00
$\alpha P_1^{O_2}$		•			0.0	0.01	0.0000	1.00
$\alpha P_2^{O_2}$		•			0.0	0.01	0.0000	1.00
$\alpha P_0^{wCO_2}$			•		$R_0^{wCO_2}$	0.1	0.0001	1.00
$\alpha P_1^{wCO_2}$			•		0.0	0.01	0.0000	1.00
$\alpha P_2^{wCO_2}$			•		0.0	0.01	0.0000	1.00
$\alpha P_0^{sCO_2}$				•	$R_0^{sCO_2}$	0.1	0.0000	1.00
$\alpha P_1^{sCO_2}$				•	0.0	0.01	0.0000	1.00
$\alpha P_2^{sCO_2}$				•	0.0	0.01	0.0000	1.00
λ_{sh}^{SIF} [nm]	•				0.0	0.01	0.0001	1.00
λ_{sq}^{SIF} [nm]	•				0.0	0.01	0.0002	0.94
$\lambda_{sh}^{O_2}$ [nm]		•			0.0	0.01	0.0000	1.00
$\lambda_{sq}^{O_2}$ [nm]		•			0.0	0.01	0.0000	1.00
$ILS_{sq}^{O_2}$		•			1.0	0.01	0.0000	1.00
$\lambda_{sh}^{wCO_2}$ [nm]			•		0.0	0.01	0.0000	1.00
$\lambda_{sq}^{wCO_2}$ [nm]			•		0.0	0.01	0.0000	1.00
$ILS_{sq}^{wCO_2}$			•		1.0	0.01	0.0000	1.00
$\lambda_{sh}^{sCO_2}$ [nm]				•	0.0	0.01	0.0000	1.00
$\lambda_{sq}^{sCO_2}$ [nm]				•	0.0	0.01	0.0000	1.00
$ILS_{sq}^{sCO_2}$				•	1.0	0.01	0.0000	1.00
SIF [$mW/m^2/sr/nm$]	•				0.0	10.0	0.29	1.00
p_s [p_0]	•	•	•	•	0.2	1.0	0.002	1.00
τ_s	•	•	•	•	0.01	0.1	0.0001	1.00
$\mathring{A}$	•	•	•	•	4.0	2.0	0.29	0.98
H_2O L_0 [ppm]			•	•	ECMWF	2179.9	497.5	0.84
H_2O L_1 [ppm]			•	•	ECMWF	2186.9	849.8	0.55
H_2O L_2 [ppm]			•	•	ECMWF	1066.0	415.2	0.59
H_2O L_3 [ppm]			•	•	ECMWF	205.4	151.4	0.21
H_2O L_4 [ppm]			•	•	ECMWF	2.67	2.59	0.00
CO_2 L_0 [ppm]			•	•	SECM2016	21.8	6.5	0.65
CO_2 L_1 [ppm]			•	•	SECM2016	14.1	4.3	0.29
CO_2 L_2 [ppm]			•	•	SECM2016	12.7	6.1	0.27
CO_2 L_3 [ppm]			•	•	SECM2016	12.0	5.9	0.42
CO_2 L_4 [ppm]			•	•	SECM2016	16.8	9.9	0.60
XH_2O [ppm]					ECMWF	898.2	9.2	2.2
XCO_2 [ppm]					SECM2016	10.0	1.0	2.2

3.1.5. A Priori Error Covariance Matrix $\mathbf{S}_a$

The a priori error covariance matrix defines the uncertainties of the a priori state vector elements and their correlations. Its dimensionality is $n \times n$. Except for the CO_2 and H_2O profile layers, we assume $\mathbf{S}_a$ to be diagonal. As described by Reuter et al. [30], we compute the CO_2 layer-to-layer covariances by comparing randomly chosen SECM2016 profiles with corresponding CT2016 model profiles. The CO_2 layer variances have been up-scaled so that the a priori XCO_2 uncertainty becomes 10 ppm (1 ppm $\widehat{=}$ 2.5‰ without scaling). This ensures retrievals to be dominated by the measurement but not the a priori. We estimated the H_2O layer-to-layer covariances by analyzing H_2O day-to-day variations of ECMWF analysis profiles. CO_2 and H_2O a priori error covariances are shown in Figures 4 and 5. All other (diagonal) elements of $\mathbf{S}_a$ are listed in row $\sigma\vec{x}_a$ of Table 1.

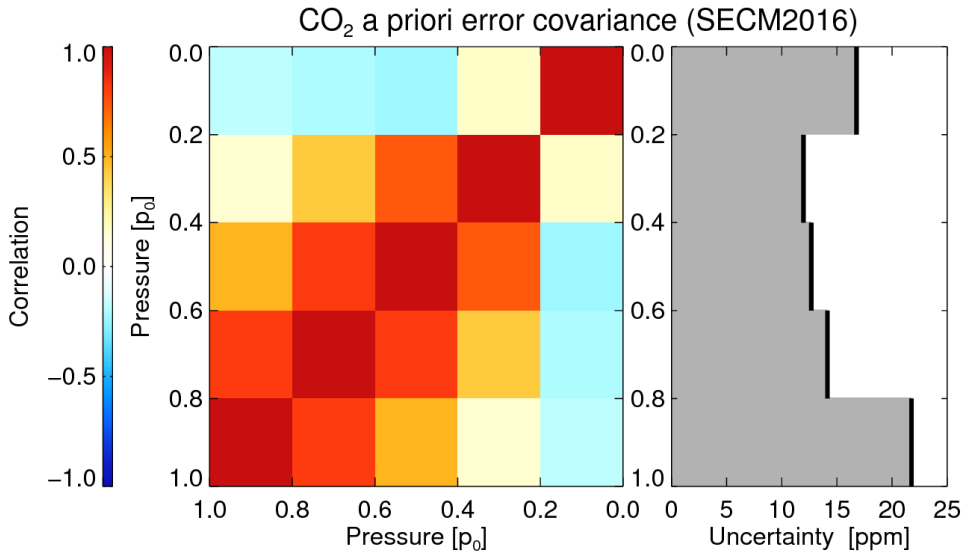

Figure 4. CO_2 a priori error covariance computed from randomly chosen SECM2016 profiles and corresponding CT2016 profiles. The CO_2 layer variances have been up-scaled so that the a priori XCO_2 uncertainty becomes 10 ppm (1 ppm without scaling). **Left**: Layer-to-layer correlation matrix of the a priori uncertainty. **Right**: 1σ a priori uncertainty.

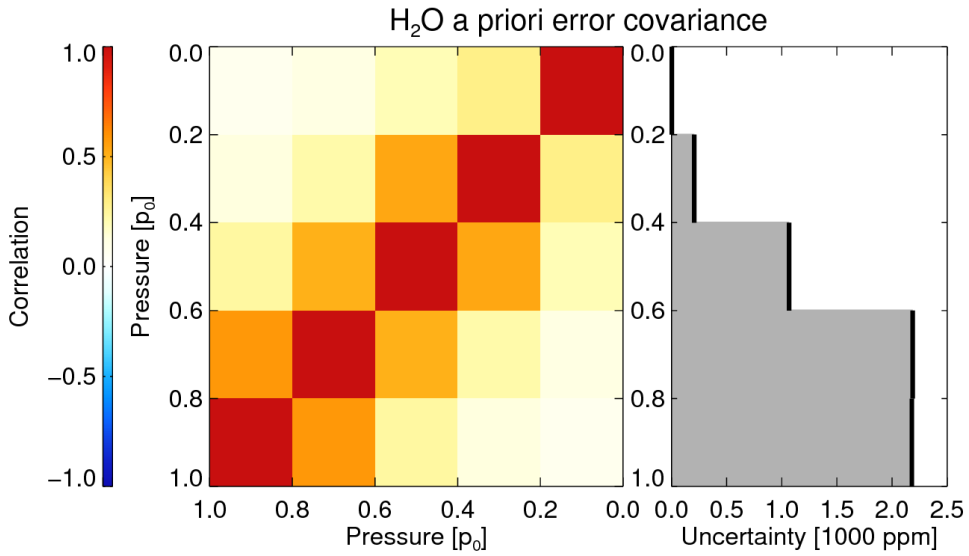

Figure 5. As Figure 4 but for H_2O and estimated from day-to-day variations of ECMWF analysis profiles (without variance scaling as done for CO_2).

3.1.6. Jacobian matrix **K**

The Jacobian matrix includes the first order derivatives of the forward model with respect to all state vector elements and has a dimensionality of $m \times n$. A measurement can only include information on those state vector elements which have sufficiently linearly independent derivatives. Figure 6 illustrates the content of a typical example of a Jacobian matrix. Note that the sensitivity to SIF has artificially been set to zero in the O_2 fit window in order to ensure, that the SIF information solely comes from the SIF fit window and misinterpretations with scattering parameters are avoided [29].

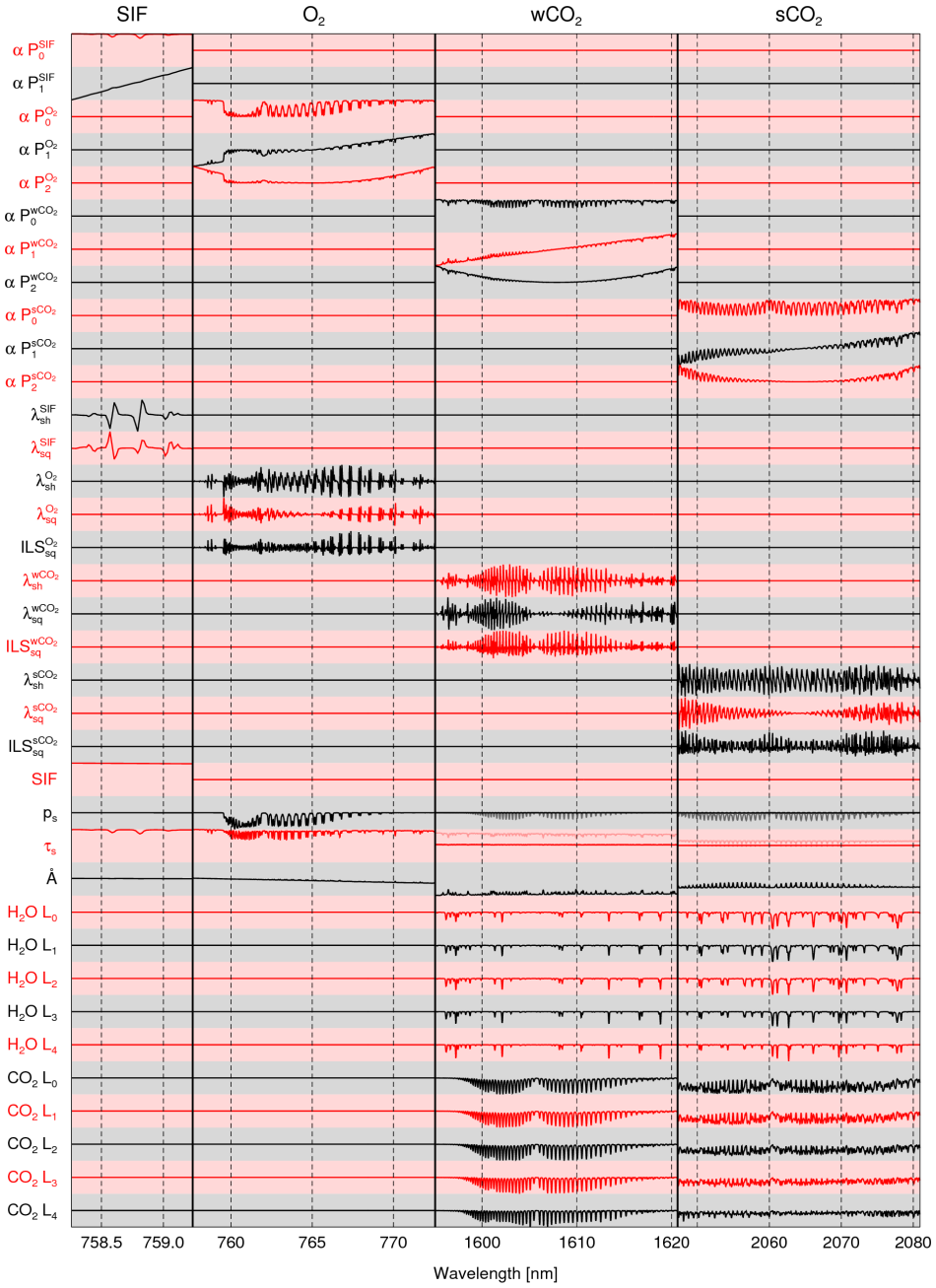

Figure 6. Jacobian matrix computed with FOCAL for the geophysical *Rayleigh* scenario and the *3-Scat* retrieval setup. Within the CO2 fit windows, an additional line in light colors shows the partial derivatives according to τ_s and p_s scaled by a factor of 10 and 20, respectively.

3.1.7. Parameter Vector $\vec{b}$

The state vector includes only a small subset of geophysical and instrumental properties that influence a simulated radiance measurement. All these additional properties are assumed to be known and form the parameter vector $\vec{b}$.

The observation geometry (particularly, the solar and satellite zenith angles θ_0 and θ), Earth/Sun distance, Doppler shifts, ILS, measurement wavelength grid, etc. are used as provided or calculated from data in the satellite L1b orbit files. Atmospheric temperature, pressure, and dry-air sub-column profiles are obtained from ECMWF analysis data. Gaseous absorption cross sections are calculated from NASA's (National Aeronautics and Space Administration) tabulated absorption cross section database ABSCO v4.0 (H_2O) and v5.0 (O_2 and CO_2) [32].

We use a high resolution solar irrandiance spectrum (F_0) which we generated by fitting the solar irradiance spectrum of Kurucz [33] with the high resolution solar transmittance spectrum used by O'Dell et al. [12], a forth order polynomial, and a Gaussian ILS. The used solar induced chlorophyll fluorescence irradiance spectrum (F^0_{SIF}) has been obtained from the publication of Rascher et al. [34] and scaled to 1.0 $mW/m^2/sr/nm$ at 760 nm. In order to account for OCO-2 measuring one polarization direction only, we divided the solar and the chlorophyll fluorescence irradiance spectrum by a factor of two.

All RT simulations are performed at a high resolution wavelength grid (not to be confused with the measurement wavelength grid) with a sampling distance of 0.001 nm for the SIF and the O_2 fit window and 0.005 nm for both CO_2 fit windows.

3.1.8. A Posteriori Error Covariance Matrix $\hat{\mathbf{S}}$

Once convergence is achieved, the a posteriori error covariance matrix includes the a posteriori uncertainties of the retrieved state vector elements and their correlations. It has a dimensionality of $n \times n$.

3.1.9. Convergence

We define that convergence is achieved when the state vector increment is small compared to the a posteriori error. Specifically, we stop iterating once:

$$\frac{1}{n}\left[(\vec{x}_i - \vec{x}_{i-1})^T\, \hat{\mathbf{S}}^{-1}\, (\vec{x}_i - \vec{x}_{i-1})\right] < 0.2. \tag{34}$$

Additionally, we test if χ^2 is smaller than 2. The maximum number of allowed iterations is 15.

3.2. Inversion Experiments

In order to asses FOCAL's theoretical capabilities (primarily in retrieving XCO_2, XH_2O, and SIF), we confront it with radiance measurements simulated with the accurate RT code SCIATRAN [35]. The performed analyses can be understood also as test of the suitability of the approximations made in FOCAL's RT and of the retrieval setup. Hereby, we primarily concentrate on scattering related errors and analyze the systematic and stochastic, i.e., the a posteriori errors of several different retrieval setups and geophysical scenarios.

We are not aiming to comprehensively cover the majority of potential geophysical scenarios, because the final quality depends on the full retrieval scheme including, e.g., potential instrument and forward model errors and different post-filtering capabilities. The aim of the inversion experiments is rather to identify a promising candidate retrieval setup serving as starting point for the development of a full retrieval scheme and its application to actually measured OCO-2 data. This is presented in part 2 of this publication [25] which also quantifies the final quality of the retrieval by comparing retrievals of actually measured data with independent ground truth measurements.

3.2.1. Retrieval Setups

The baseline retrieval setup is described in Section 3.1. As this setup accounts for scattering with three scattering related state vector elements (pressure, i.e., height of the scattering layer p_s, scattering optical thickness τ_s, and Ångström exponent $\mathring{A}$), it is referred to as *3-Scat* setup in the following. All other tested retrieval setups are descendants of this setup. The *4-Scat* setup has an extended state vector, additionally fitting the fraction of radiation scattered into the hemisphere in forward direction (f in Equation (15)). The *0-Scat* setup equals an absorption only retrieval; this means, the state vector does not include any scattering related parameters and the fit is limited to the CO_2 fit windows. The *3-Scat-O_2* setup equals the baseline setup except for scattering parameter derivatives which have artificially been set to zero in the CO_2 bands in order to ensure that the scattering information solely comes from the O_2 band. Accordingly, the *3-Scat-CO_2* setup ensures that the scattering information solely comes from the CO_2 bands. The scenarios *3-Scat-synth* and *0-Scat-synth* use a synthetic a priori error covariance matrix for the CO_2 profile as proposed by Reuter et al. [30] but with a correlation length of 1.0 p_0 instead of 0.3 p_0. The scenarios *3-Scat-stiff* and *0-Scat-stiff* use a similar synthetic a priori error correlation matrix but computed with a correlation length of 100 p_0. This "stiffens" the a priori error covariance matrix so that the departure from the a priori profile becomes basically proportional to the uncertainty profile. For these scenarios, the a priori error covariance matrix of the H_2O profile has been stiffened in the same way.

3.2.2. Scenarios

The geophysical *baseline* scenario has a spectrally flat albedo of 0.2, 0.2, 0.1, and 0.05 in the SIF, O_2, wCO_2, and sCO_2 fit window; values which have also been used by, e.g., Bovensmann et al. [4]. It does not include chlorophyll fluorescence, scattering by aerosols, clouds, or Rayleigh. Its temperature, pressure, and water vapor ($XH_2O = 3031\,\text{ppm} \mathrel{\widehat{=}} 19.52\,\text{kg/m}^2$) profiles are taken from an ECMWF analysis of 28 August 2015, 12:00 UTC, 9°E, 53°N. Its CO_2 profile is calculated with SECM2016 and corresponds to an XCO_2 value of about 395 ppm. Note that ECMWF and SECM2016 are also used to compute the first guess and a priori H_2O and CO_2 profiles (Table 1). All other scenarios are descendants of the *baseline* scenario.

Each scenario is analyzed for three solar zenith angles (20°, 40°, and 60°) and for two directions of polarization (parallel and perpendicular to the SPP). The satellite zenith angle is set to 0° (nadir).

The *SIF* scenario adds 1 $\text{mW/m}^2\text{/sr/nm}$ chlorophyll fluorescence at 760 nm to the simulated measurement of the *baseline* scenario. The *XCO_2+6 ppm* scenario has an increased CO_2 concentration of 15 ppm, 10 ppm, and 5 ppm in the three lowermost layers, so that the column-average concentration is enhanced by 6 ppm.

All scattering related scenarios are more complex for the retrieval because of FOCAL's scattering approximations. The *Rayleigh* scenario adds Rayleigh scattering to the baseline scenario; the Rayleigh optical thickness at 760 nm for this scenario is about 0.026. *Rayleigh+Aerosol BG* additionally includes a (primarily) stratospheric background aerosol with an AOT (aerosol optical thickness at 760 nm) of 0.019 (0.003 at 1600 nm and 0.001 at 2050 nm). *Rayleigh+Aerosol cont* adds a continental aerosol to the boundary layer so that the total AOT becomes 0.158 (0.060 at 1600 nm and 0.037 at 2050 nm). *Rayleigh+Aerosol urban* adds a strong contamination with urban aerosol to the boundary layer and the total AOT becomes 0.702 (0.245 at 1600 nm and 0.151 at 2050 nm).

The scenarios *Rayleigh+Dark surface*, *Rayleigh+Bright surface*, and *Rayleigh+Ocean glint* distinguish from the *Rayleigh* scenario only by their surface reflection properties. *Rayleigh+Dark surface* and *Rayleigh+Bright surface* correspond to the *Rayleigh* scenario but with an albedo multiplied with 0.7 and 1.4, respectively. The *Rayleigh+Ocean glint* scenario deviates from the assumption of a Lambertian surface bidirectional reflectance distribution function (BRDF); it includes an ocean surface at a wind speed of 5 m/s, 37° to the solar principal plane (SPP). Additionally, the satellite zenith angle of this scenario is set to 0.75 times the solar zenith angle so that the satellite looks near the glint spot of specular reflectance.

Two cloud scenarios (*Rayleigh+Aerosol BG+Water cloud* and *Rayleigh+Aerosol BG+Ice cloud*) add a sub-visible water or ice cloud to the *Rayleigh+Aerosol BG* scenario. The water cloud has a height of 3 km, droplets with an effective radius of 12 µm, and a COT (cloud optical thickness at 500 nm) of 0.039. The ice cloud is made of fractal particles with an effective radius of 50 µm, has a height of 8 km, and a COT of 0.033.

Appendix B lists important input parameters which have been used to perform the SCIATRAN RT calculations for all scenarios.

3.2.3. Results

Primarily, we are interested in XCO_2 retrieval results of high quality; the correct retrieval of other state vector elements is less important as long as the XCO_2 quality is not affected. Figure 7 summarizes the systematic errors and stochastic uncertainties of the retrieved XCO_2 for all retrieval setups and geophysical scenarios.

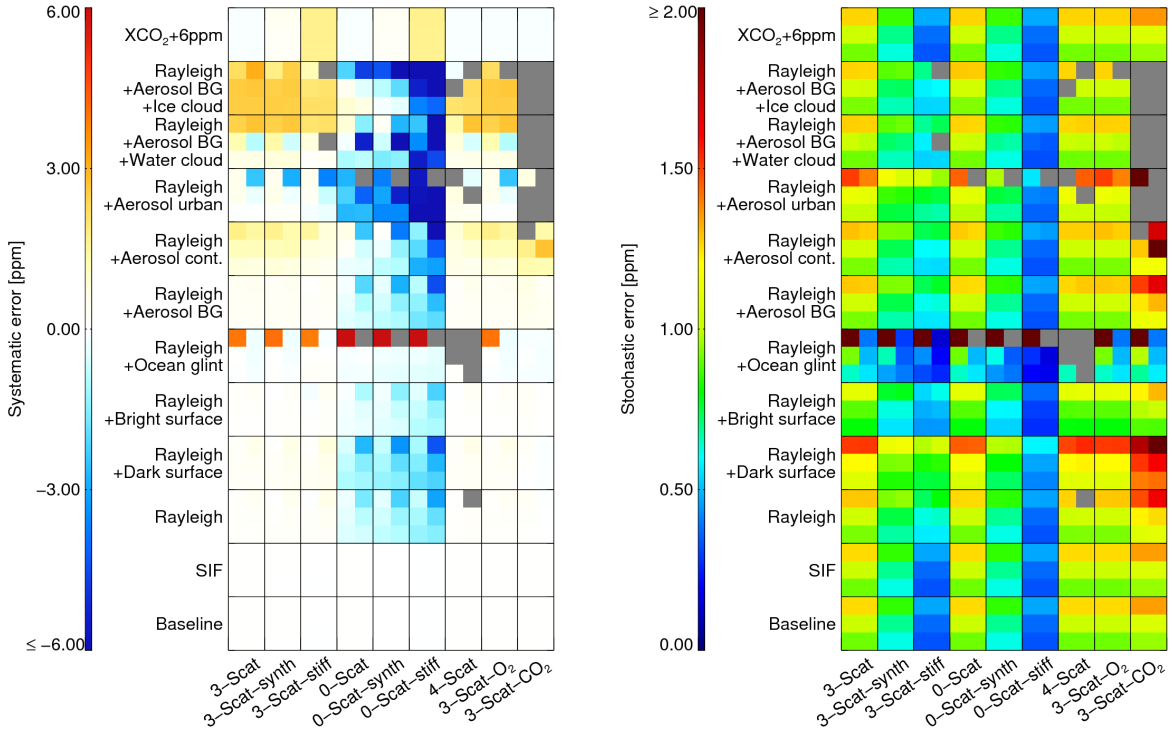

Figure 7. Error characteristics of nine retrieval setups and twelve geophysical scenarios. Each box includes six sub-boxes representing polarization parallel (left) and perpendicular (right) to the SPP as well as three solar zenith angles (20°, 40°, and 60°, from bottom to top). Gray boxes represent not converging retrievals. **Left**: Systematic error (retrieved minus true XCO_2). **Right**: Stochastic uncertainty as reported by the optimal estimation retrieval.

The *baseline* scenario is mainly to ensure consistency of the RT used to simulate the measurements (SCIATRAN) and the RT of the retrieval (FOCAL). Additionally, the *baseline* scenario allows estimates of the retrieval's noise error. With SCIATRAN, it is not simply possible to simulate FOCAL's scattering approximations, that is why this scenario excludes scattering. The systematic errors of the *baseline* scenario are always very small (0.03 ppm at maximum), which confirms the RT consistency in the absorption only case and ensures that, e.g., the number of particles is basically identical in the SCIATRAN and the FOCAL "world".

The systematic errors of the *SIF* scenario are not larger than for the *baseline* scenario, because i) SIF is solely determined from the SIF fit window and ii) there is no SIF flux emitted in the CO_2 fit windows.

A more complex case for FOCAL is the *Rayleigh* scenario, because Rayleigh scattering takes place in the entire atmospheric column with a peanut-shaped SPF. This means, it cannot be expected that FOCAL is able to perfectly fit the simulated measurement. Figure 8 (top) shows a spectral fit in all fit windows but with a state vector not including any scattering parameter, so that the geophysical results (e.g., XCO_2) become identical with those of the *0-Scat* setup.

Not surprisingly, the residual in the O_2 fit window becomes large compared to the simulated measurement noise ($\chi_{O_2} = 6.825$). The residuals in the CO_2 fit windows are already small compared to the instrumental noise even without fitting scattering parameters ($\chi_{wCO_2} = 0.026$, $\chi_{sCO_2} = 0.049$). This is only partly explained by Rayleigh scattering having an Ångström exponent of four and, therefore, a much smaller scattering optical thickness at longer wavelengths. It also indicates that disentangling scattering parameters and CO_2 concentration from measurements in the CO_2 fit windows may be difficult. In other words, most of the scattering information must be imprinted in the residual of the O_2 fit window. This is also why the results of the *3-Scat-*O_2 setup are similar to the *3-Scat* setup and why the *3-Scat-*CO_2 retrievals are often not converging (Figure 7).

Allowing the *3-Scat* retrieval setup to fit the scattering parameters p_s, τ_s, and $\mathring{A}$, reduces the O_2 residual to become typically four times smaller than expected from instrumental noise ($\chi_{O_2} = 0.250$, Figure 8, middle). Simultaneously, the XCO_2 error reduces from -0.43 ppm to 0.10 ppm (-0.89 ppm and 0.16 ppm for perpendicular polarization).

All other scattering related scenarios are even more "complicated" for FOCAL because different particles contribute to scattering. For example, cloud particles have different properties like height or Ångström exponent as aerosol particles, but FOCAL can only retrieve one effective height and one effective Ångström exponent. Additionally, the SPFs of aerosols and clouds are less isotropic. Therefore, the residuals (Figure 8, bottom) and more importantly, the systematic errors typically increase for these scenarios (Figure 7, left).

Figure 9 shows the retrieved scattering parameters for the *3-Scat* setup and a set of scattering related plus the baseline scenario. As the baseline scenario does not include any scattering, the retrieved p_s and $\mathring{A}$ are close to their a prior values and have a large a posteriori uncertainty. Consistent with the expectations, the retrieved effective Ångström exponent is close to four (about 3.8) for the Rayleigh scenario and reduces to 2.8–3.6 for the aerosol and 2.1–2.6 for cloud scenarios. This means the scattering optical thickness at longer wavelengths increases relative to the shorter wavelengths. Rayleigh scattered light is unpolarized in forward and backward scattering direction but polarized perpendicular to the incident beam for scattering angles of 90°. For this reason, the retrieved τ_s is always larger for the polarization direction perpendicular to the SPP. As expected, this effect is more/less pronounced for larger/smaller solar zenith angles (not shown). In contrast to the *3-Scat* and *4-Scat* setups, the *0-Scat* retrievals cannot fit τ_s which results in a larger polarization dependency of the resulting systematic errors (Figure 7, left).

As shown in Figure 9, the highest scattering optical thicknesses at 760 nm are obtained for the urban aerosol and the cloud scenarios. However, the quantitative interpretation of the retrieved values of τ_s and p_s is difficult because they are effective values representing all kinds of scattering in the atmospheric column. Additionally, τ_s and p_s may not be perfectly independent because light path modifications are expected to become larger when enhancing the height of the scattering layer. It can be observed that the retrieved values of τ_s are generally smaller than the scattering optical thicknesses computed by SCIATRAN (Section 3.2.2). This is expected because of the different SPFs assumed by SCIATRAN and FOCAL. Especially for Mie scattering of cloud and aerosol particles, the SCIATRAN simulations use SPFs with a distinct forward peak contributing to the total scattering optical thickness. FOCAL, however, interprets scattering in forward direction as transmission (not contributing to τ_s). This means, τ_s is best comparable for the *Rayleigh* scenario with a SPF without forward peak.

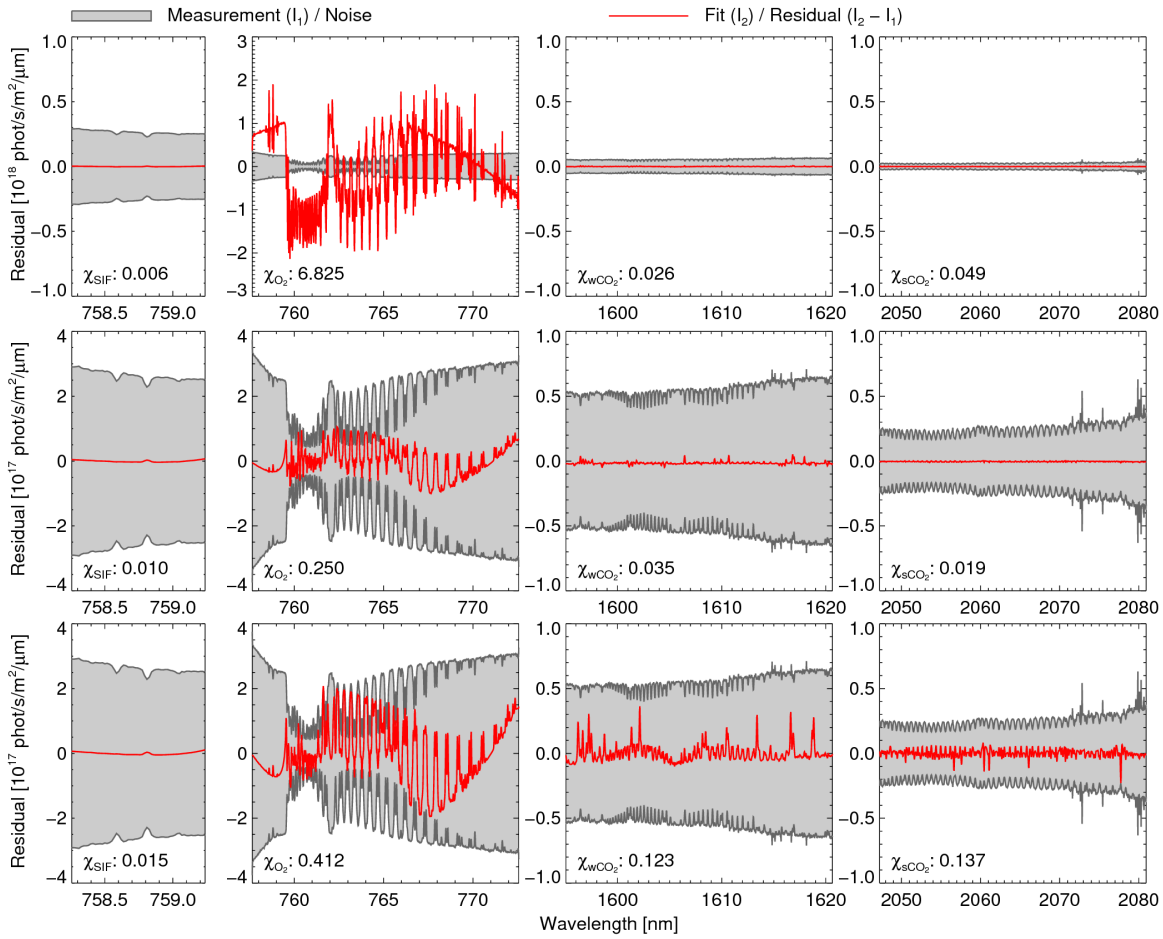

Figure 8. As Figure 3 (bottom) but for the *Rayleigh* scenario and the *0-Scat* setup (**top**), the *Rayleigh* scenario and the *3-Scat* setup (**middle**), and the *Rayleigh+Aerosol BG+Water cloud* scenario and the *3-Scat* setup (**bottom**).

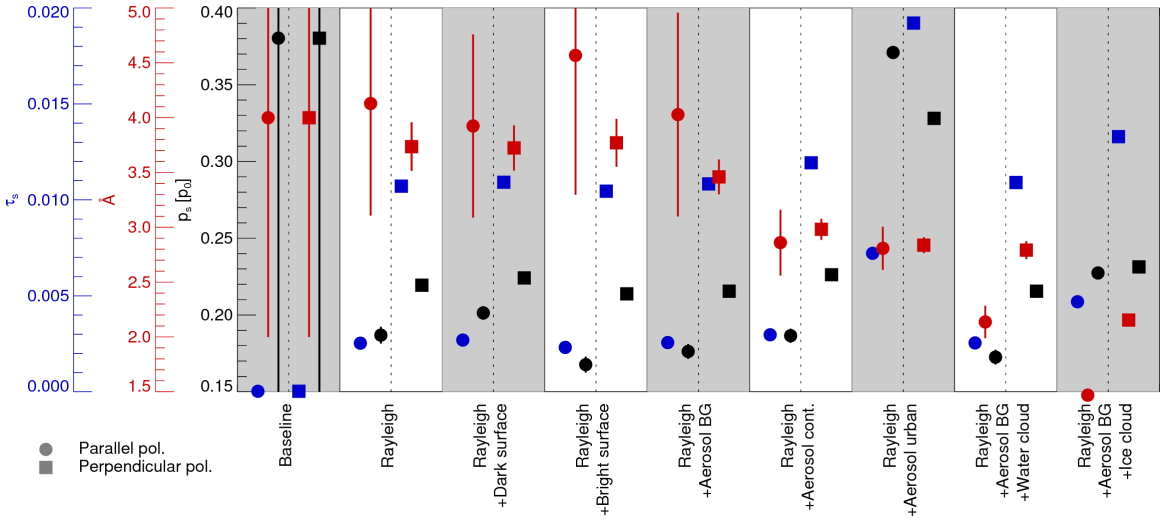

Figure 9. Retrieved scattering optical thickness, Ångström exponent, and height of the scattering layer for the *3-Scat* setup and the scenarios (θ_0 = 40°): *baseline*, *Rayleigh*, *Rayleigh+Dark surface*, *Rayleigh+Bright surface*, *Rayleigh+Aerosol BG*, *Rayleigh+Aerosol cont*, *Rayleigh+Aerosol urban*, *Rayleigh+Aerosol BG+Water cloud*, and *Rayleigh+Aerosol BG+Ice cloud*.

The scenarios *Rayleigh*, *Rayleigh+Dark surface*, and *Rayleigh+Bright surface* differ by their surface albedo. However, the retrieved scattering parameters show little differences because in FOCAL these parameters represent (within the limits of the made assumptions) approximations of real geophysical quantities.

Applying FOCAL to the *Rayleigh+Ocean glint* scenario with a highly non-Lambertian surface BRDF results in systematic XCO_2 and XH_2O errors usually comparable to the *Rayleigh* scenario (Figures 7 and 10, left) except for solar zenith angles of 60° and polarization parallel to the SPP. In near-glint geometry, specular reflectance dominates the radiation field but with increasing solar zenith angle the reflected radiation becomes more and more polarized. As a result the direct photon path often dominates (if not observing parallel polarization at large solar zenith angles) and an imperfect parameterization of scattering becomes less important. The domination of the direct photon path also results in a larger total radiance and, correspondingly, smaller stochastic errors in perpendicular polarization (Figures 7 and 10, right). The larger systematic XCO_2 errors of about 4 ppm at 60° and parallel polarization are a result of the poor surface reflectivity in this observation geometry and associated with large stochastic errors of about 8 ppm and little error reduction (analog for XH_2O). This means, applied to real measurements, such retrievals would most certainly be filtered during post processing. Note that due to the non-Lambertian surface, the retrieved albedo may have values larger than one.

Figure 7 (right) shows that the shape of the CO_2 a priori error covariance matrix can considerably influence the stochastic XCO_2 a posteriori uncertainty, even though the a priori XCO_2 uncertainty has not been changed. Stiffening the covariance matrix by enhancing the layer-to-layer correlations as done for the *synth* and *stiff* setups (Figures 11 and 12), reduces the stochastic XCO_2 uncertainty from typically about 1 ppm to 0.7 ppm (*synth*) and 0.4 ppm to 0.6 ppm (*stiff*), which does not necessarily mean that results actually improve.

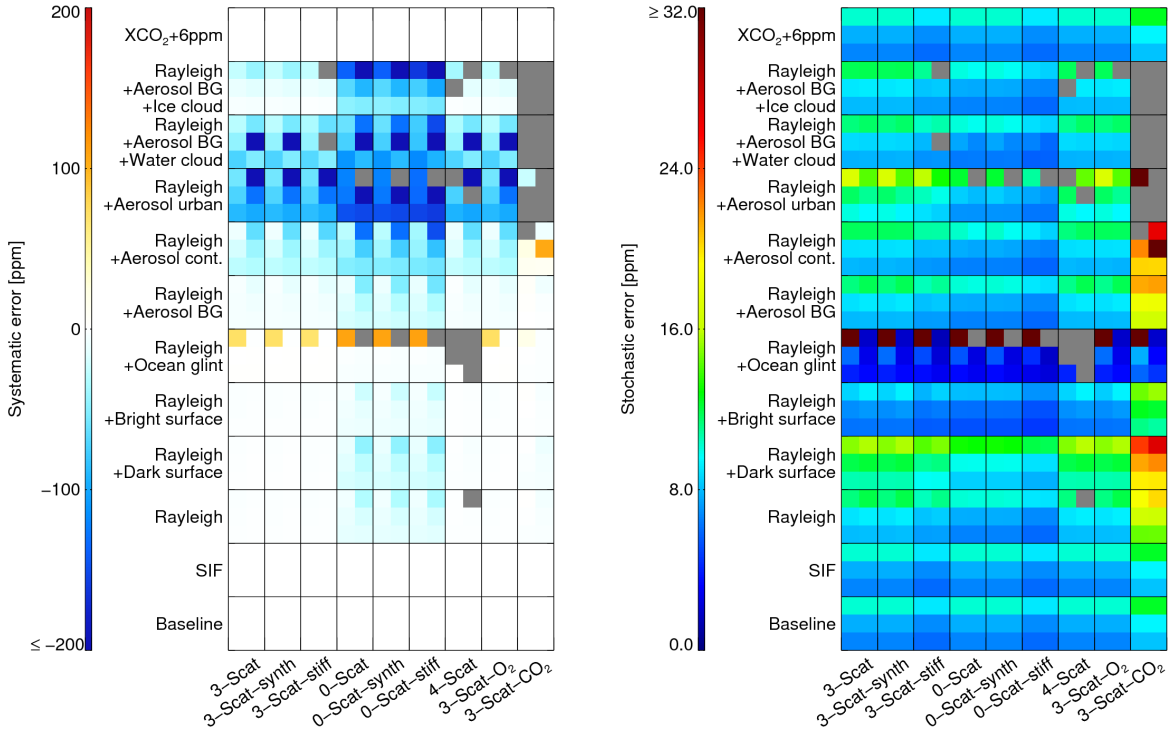

Figure 10. As Figure 7 but for XH_2O.

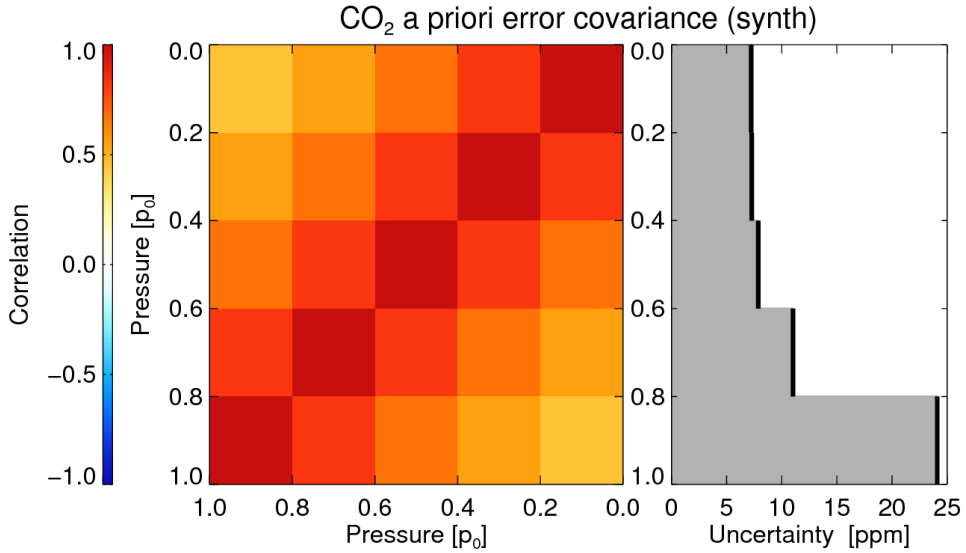

Figure 11. As Figure 4 but for a synthetic a priori error covariance matrix as proposed by Reuter et al. [30] but with a correlation length of 1.0 p_0.

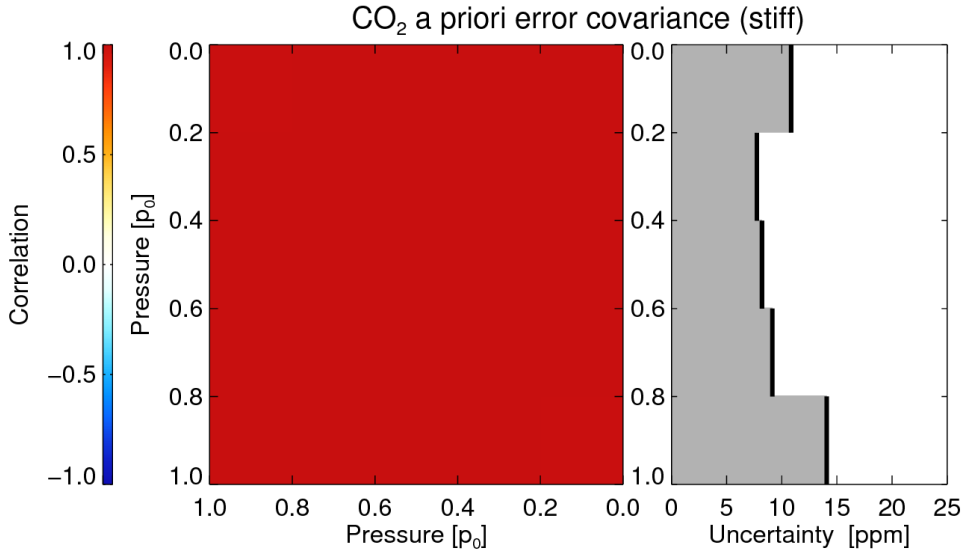

Figure 12. Same as Figure 4 but for a synthetic a priori error correlation matrix as proposed by Reuter et al. [30] but with a correlation length of 100 p_0.

Except for the *XCO2+6 ppm* scenario, the systematic errors of the *3-Scat*, *3-Scat-synth*, and *3-Scat-stiff* setups are very similar. This is not the case for the *0-Scat*, *0-Scat-synth*, and *0-Scat-stiff* setups for which the systematic errors increase with stiffness of the CO_2 a priori error covariance matrix. Apparently, the (loose) profile retrieval of the *0-Scat* scenario happens to somewhat compensate light path related errors. In the case of the *3-Scat* setups, the scattering parameters are doing this job. Figure 13 shows, that the largest deviations of the retrieved profiles from the true profile (a priori) indeed occur for the *0-Scat* setup.

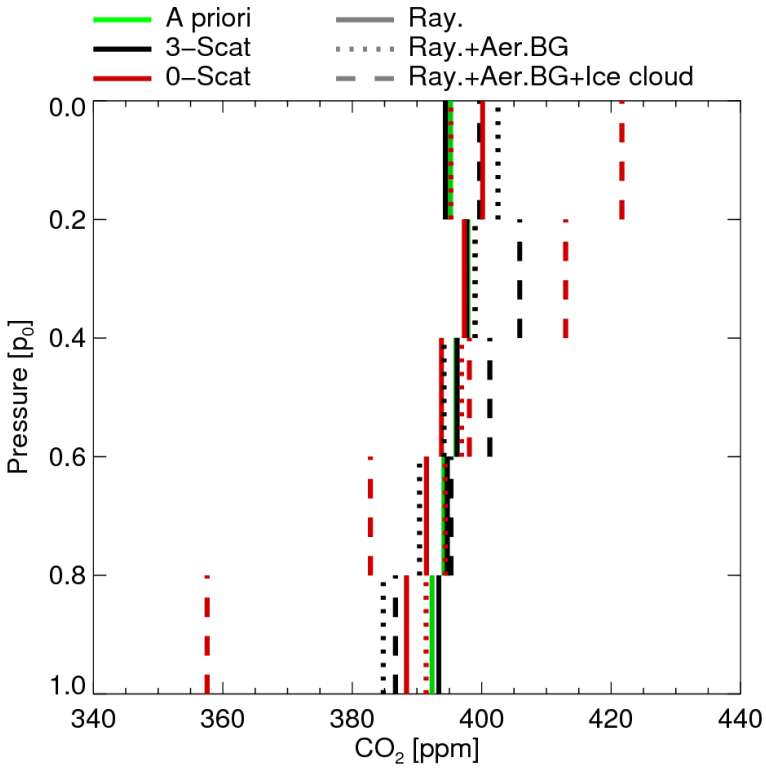

Figure 13. Retrieved and a priori CO_2 profiles for the *0-Scat* and *3-Scat* retrieval setups and the geophysical scenarios *Rayleigh*, *Rayleigh+Aerosol BG*, and *Rayleigh+Aerosol BG+Ice cloud* (θ_0 = 40°, perpendicular polarization).

The degree of freedom for the CO_2 profile is about 2.2 for the *3-Scat* setup and reduces to 1.8 for the *3-Scat-synth* and 1.0 for the *3-Scat-stiff* setup. The degree of freedom for the H_2O profile reduces from 2.2 for the *3-Scat* setup to 1.0 for the *3-Scat-stiff* setup. Additionally, the column averaging kernels (AKs) change and show larger deviations from unity; specifically, as illustrated in Figure 14, the XCO_2 AK increases to about 1.2 in the boundary layer and reduces to 0.6 in the stratosphere. As a result, the systematic error (in this particular case, the smoothing error) increases for the *stiff* setups to about 1.6 ppm (Figure 7, left).

As illustrated in Figure 10, scattering related systematic XH_2O errors are usually negative and larger for the *0-Scat* setups. Stiffening the H_2O a priori error covariance matrix has little influence on the systematic or stochastic error which is usually about 10 ppm. SIF is almost not influenced by the mostly low scattering optical thicknesses of the tested scenarios and the stochastic a posteriori error is usually between 0.2 and 0.3 $mW/m^2/sr/nm$ (Figure 15).

All tested retrieval setups do not have the ability to change the number of dry-air particles in the atmospheric column, e.g., by fitting the surface pressure, or a shift of the temperature profile. As a result, relative errors of the number of dry-air particles computed from the meteorological profiles directly translate into relative errors of the retrieved XCO_2 and XH_2O. For example, a 1 hPa error of the surface pressure will result in a XCO_2 error of about 0.4 ppm.

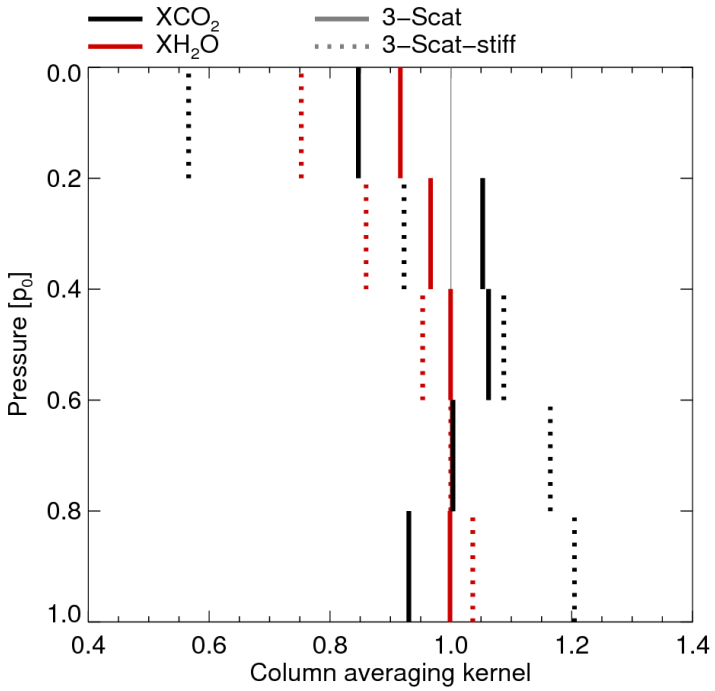

Figure 14. XCO_2 and XH_2O column averaging kernels for the *3-Scat* and *3-Scat-stiff* retrieval setups and the geophysical *Rayleigh* scenario (θ_0 = 40°, perpendicular polarization).

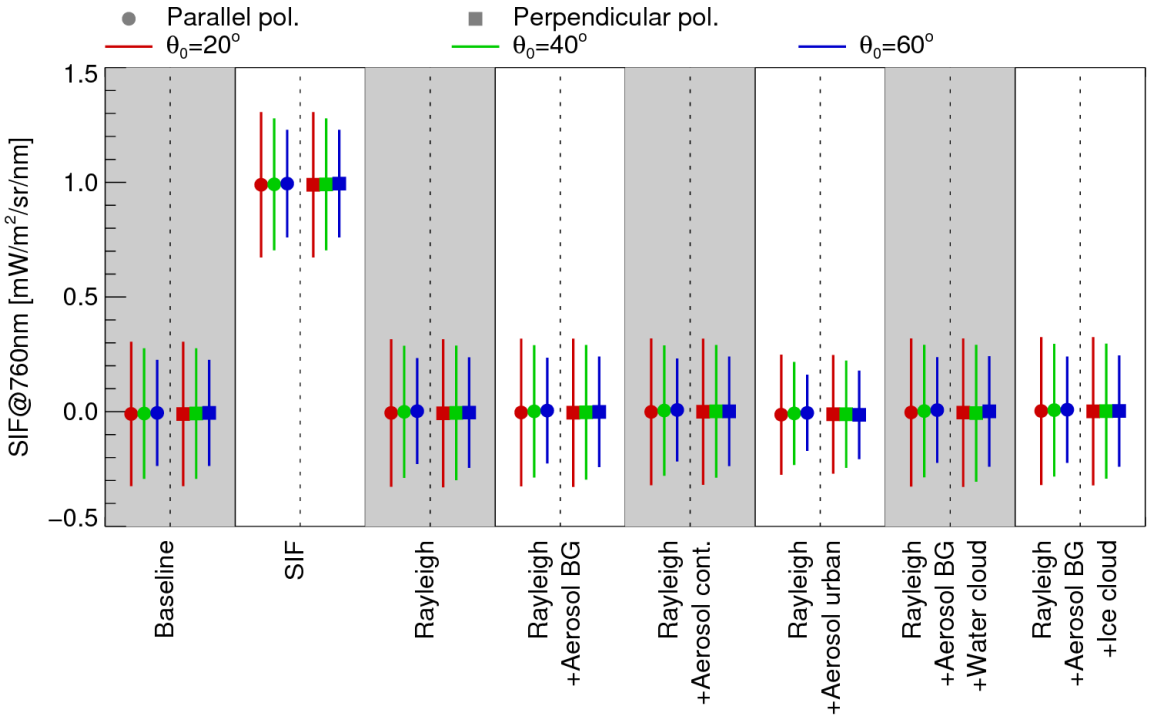

Figure 15. Retrieved solar induced chlorophyll fluorescence for the *3-Scat* retrieval setup and the geophysical *baseline*, *SIF*, and all scattering related scenarios. The error bars represent the 1σ a posteriori uncertainty.

4. Conclusions

We presented the fast atmospheric trace gas retrieval FOCAL including a RT model which approximates multiple scattering effects at an optically thin isotropic scattering layer and assessed the

potential performance of various XCO_2, XH_2O, and SIF retrieval setups for an OCO-2 like instrument. FOCAL accounts for scattering by splitting up the top of atmosphere (TOA) radiance into parts originating from direct reflection at the scattering layer or the surface and parts originating from multiple scattering of the diffuse radiant flux between scattering layer and surface. FOCAL's relatively simple approximation of the RT problem allows unphysical inputs such as negative scattering optical thicknesses or albedos. This can be an advantage when analyzing measurements including noise and assuming Gaussian a priori error statistics. FOCAL accounts for polarization only implicitly by the retrieval of a variable scattering optical thickness.

The PPDF method [e.g., 19,20] gains its computational efficiency by applying the theorem of equivalence to replace computationally expensive multiple scattering RT computations with a set of fast transmission computations. This is conceptually similar to FOCAL which uses an effective transmission function for the diffuse flux. However, different from the PPDF method, FOCAL accounts for multiple scattering by solving the geometric series of successive (flux) scattering events.

In principle, the PPDF method can simulate arbitrary SPFs. This is not possible for FOCAL which can only simulate an isotropic scattering layer. However, splitting the radiance into direct and diffuse parts can be interpreted as a SPF with a sharp forward peak and which is isotropic otherwise. This still represents typical Mie SPFs not very well but much better than an entirely isotropic SPF.

Strictly, the theorem of equivalence only applies for spectral regions with constant scattering and reflection properties [27] making the PPDF shape, e.g., depending on surface albedo. This can make it complicated to transfer scattering information from one fit window into another. Reflection and scattering properties of FOCAL are allowed to vary within the fit windows and can be used to transfer information between fit windows, e.g., via the Ångström exponent.

We confronted several different retrieval setups with simulated OCO-2 radiance measurements of a set of different geophysical scenarios, solar zenith angles, and polarization directions. Due to often relatively low systematic XCO_2 and XH_2O errors with low polarization dependency, well controlled retrieved profiles, lowest CO_2 smoothing errors, a relatively realistic a priori error correlation matrix for CO_2, and advantageous AKs, we conclude that the *3-Scat* setup is a promising candidate for further studies with measured OCO-2 data.

The *3-Scat* setup fits the OCO-2 measured radiance in four fit windows by simultaneously retrieving the following geophysical parameters: five layered CO_2 and H_2O concentration profiles, the pressure (i.e., height), scattering optical thickness at 760 nm, and the Ångström exponent of a scattering layer, SIF, and polynomial coefficients describing the spectral albedo in each fit window.

As accurate XCO_2 retrievals will probably always require a rigorous cloud and aerosol screening, we concentrated on scenarios with scattering optical thicknesses in the range of about 0.03 and 0.70.

The quality of the spectral fits in the O_2 fit window is usually 2.5 to 4 times better than expected from instrumental noise. In the CO_2 fit windows, the quality of the spectral fits is usually at least 7 times better than expected from instrumental noise and even smaller fit residuals are obtained in the SIF fit window.

Systematic errors of XCO_2 range from -2.5 ppm to 3.0 ppm and are usually smaller than ± 0.3 ppm (for the tested scenarios). The stochastic uncertainty of XCO_2 is typically about 1.0 ppm. Systematic errors of XH_2O range from -243 ppm to 0 ppm and are usually smaller than ± 6 ppm. The stochastic uncertainty of XH_2O is typically about 9 ppm. Note, 1000 ppm $\widehat{=}$ 6.44 kg/m^2 for the analyzed H_2O profiles. The degree of freedom for the retrieved five-layered CO_2 and H_2O profiles is typically 2.2. As SIF is retrieved from Fraunhofer lines in a spectral region with negligible gaseous absorption features, it can be retrieved without significant interferences with the retrieved scattering properties. The systematic SIF errors are always below 0.02 mW/m^2/sr/nm, i.e., it can be expected that instrumental or forward model effects causing an in-filling (a reduction of the line depths) of the used Fraunhofer lines will dominate the systematic errors when analyzing actually measured data. The stochastic uncertainty of SIF is usually below 0.3 mW/m^2/sr/nm.

All SCIATRAN and FOCAL RT computations have been performed with an Intel Core i7-3770 CPU with four cores running at 3.4 GHz (released in 2012). On a single core, the SCIATRAN (programmed with FORTRAN) computations of the *Rayleigh+Aerosol BG+Water cloud* scenario took about 32,000 s. This compares to 0.06 s for FOCAL (programmed with IDL) if only the spectrum and 0.11 s if also the Jacobian is computed. The convolution of spectrum and Jacobian adds 0.22 s and is, therefore, currently the main driver of the total computation time of 0.33 s needed for the forward model of the retrieval.

Especially in view of potential future satellite missions similar to CarbonSat easily exceeding one million quality-filtered cloud-free soundings per day [4,36], a gain in processing speed of this magnitude is urgently needed. Approximating for convenience that on average ten iterations are needed per sounding, results in a need for about 400 CPU cores to process such a data stream ten times faster than acquired which may reduce to 20 up-to-date CPU cores at launch date. FOCAL's computations are simple enough for an adaptation to GPU architecture with reasonable effort which has the potential for a further substantial acceleration.

Without understating the importance of analyzing synthetic measurements as presented here, the actual retrieval performance can only be assessed by analyzing measured data including, e.g., pre- and post-filtering, and all kinds of instrumental effects, which is subject to part 2 of this publication [25].

Acknowledgments: This work was in part funded by ESA/ESRIN (GHG-CCI II project), the European Union (Copernicus Climate Change Service led by ECMWF), and the State and the University of Bremen. The OCO-2 data were produced by the OCO-2 project at the Jet Propulsion Laboratory, California Institute of Technology, and obtained from the OCO-2 data archive maintained at the NASA Goddard Earth Science Data and Information Services Center. Additionally, NASA provided the absorption cross section database ABSCO. We used solar spectra made available by R. L. Kurucz and G. C. Toon and a chlorophyll fluorescence spectrum published by U. Rascher. NOAA made available the CarbonTracker CO_2 fields. ECMWF provided the used meteorological profiles.

Author Contributions: Maximilian Reuter: Design and implementation of the RT scheme and the XCO_2 satellite retrieval; design, implementation, conduction, and interpretation of the simulation experiments; writing the paper.Michael Buchwitz, Oliver Schneising, Stefan Noel, Vladimir Rozanov, Heinrich Bovensmann, John P. Burrows: Support in design of the RT scheme and the XCO_2 satellite retrieval; support in interpretation of the simulation experiments; support in writing the paper.

Conflicts of Interest: The authors declare no conflict of interest.

Appendix A

Within this appendix, we are deriving Equation (25) as approximation of Equation (1). First, we are substituting the approximations made Section 2.10 including Equations (8), (22)–(24) into Equations (17)–(21):

$$I_C \approx I_0\,\zeta_0\,\tau_s\,\frac{1}{2} \tag{A1}$$

$$I_{SD} \approx I_0\,\alpha\,(1-\zeta\,\tau_s-\zeta_0\,\tau_s+\zeta\,\zeta_0\,\tau_s^2)\,T_I^g(\tau_\downarrow,\zeta_0)\,T_I^g(\tau_\downarrow,\zeta)\,\frac{1}{1-2\,\alpha\,\tau_s\,E_2(\tau_\downarrow)\,E_3(\tau_\downarrow)} \tag{A2}$$

$$I_{CD} \approx I_0\,\alpha\,(\tau_s-\zeta_0\,\tau_s^2)\,E_2(\tau_\downarrow)\,T_I^g(\tau_\downarrow,\zeta_0)\,\frac{1}{1-2\,\alpha\,\tau_s\,E_2(\tau_\downarrow)\,E_3(\tau_\downarrow)} \tag{A3}$$

$$I_{SI} \approx I_0\,\alpha\,\zeta_0\,(\tau_s-\zeta\,\tau_s^2)\,E_3(\tau_\downarrow)\,T_I^g(\tau_\downarrow,\zeta)\,\frac{1}{1-2\,\alpha\,\tau_s\,E_2(\tau_\downarrow)\,E_3(\tau_\downarrow)} \tag{A4}$$

$$I_{CI} \approx I_0\,\alpha\,\zeta_0\,\tau_s^2\,E_2(\tau_\downarrow)\,E_3(\tau_\downarrow)\,\frac{1}{1-2\,\alpha\,\tau_s\,E_2(\tau_\downarrow)\,E_3(\tau_\downarrow)} \tag{A5}$$

$$I_{SIF} \approx \frac{F_{SIF}^0}{\pi}\,(1-\zeta\,\tau_s)\,T_I^g(\tau_\downarrow+\tau_\uparrow,\zeta) \tag{A6}$$

Preparing some terms used for the Taylor series approximation of Equation (1). Function values at $\tau_s = 0$:

$$I_C|_{\tau_s=0} = 0 \quad \text{(A7)}$$

$$I_{SD}|_{\tau_s=0} = I_0\, \alpha\, T_I^g(\tau_\downarrow, \zeta_0)\, T_I^g(\tau_\downarrow, \zeta) \quad \text{(A8)}$$

$$I_{CD}|_{\tau_s=0} = 0 \quad \text{(A9)}$$

$$I_{SI}|_{\tau_s=0} = 0 \quad \text{(A10)}$$

$$I_{CI}|_{\tau_s=0} = 0 \quad \text{(A11)}$$

$$I_{SIF}|_{\tau_s=0} = \frac{F_{SIF}^0}{\pi}\, T_I^g(\tau_\downarrow + \tau_\uparrow, \zeta) \quad \text{(A12)}$$

First derivatives according to τ_s at $\tau_s = 0$:

$$\left.\frac{\partial I_C}{\partial \tau_s}\right|_{\tau_s=0} = I_0\, \zeta_0\, \frac{1}{2} \quad \text{(A13)}$$

$$\left.\frac{\partial I_{SD}}{\partial \tau_s}\right|_{\tau_s=0} = I_0\, \alpha\, T_I^g(\tau_\downarrow, \zeta_0)\, T_I^g(\tau_\downarrow, \zeta)\, \left(2\, \alpha\, E_2(\tau_\downarrow)\, E_3(\tau_\downarrow) - \zeta - \zeta_0\right) \quad \text{(A14)}$$

$$\left.\frac{\partial I_{CD}}{\partial \tau_s}\right|_{\tau_s=0} = I_0\, \alpha\, E_2(\tau_\downarrow)\, T_I^g(\tau_\downarrow, \zeta_0) \quad \text{(A15)}$$

$$\left.\frac{\partial I_{SI}}{\partial \tau_s}\right|_{\tau_s=0} = I_0\, \alpha\, \zeta_0\, E_3(\tau_\downarrow)\, T_I^g(\tau_\downarrow, \zeta) \quad \text{(A16)}$$

$$\left.\frac{\partial I_{CI}}{\partial \tau_s}\right|_{\tau_s=0} = 0 \quad \text{(A17)}$$

$$\left.\frac{\partial I_{SIF}}{\partial \tau_s}\right|_{\tau_s=0} = -\frac{F_{SIF}^0}{\pi}\, \zeta\, T_I^g(\tau_\downarrow + \tau_\uparrow, \zeta) \quad \text{(A18)}$$

First order Taylor series approximation of Equation (1) at $\tau_s = 0$ and substituting Equation (13) yields Equation (25).

$$I \approx I|_{\tau_s=0} + \left.\frac{\partial I}{\partial \tau_s}\right|_{\tau_s=0} \tau_s \quad \text{(A19)}$$

Appendix B

In the following, we list important input parameters of the performed SCIATRAN RT calculations. More information on SCIATRAN can be found in the publication of Rozanov et al. [35].

Table A1. General parameters of radiative transfer (RT) calculations.

Sphericity	plane-parallel
RT solver	vector discrete ordinates method
Number of streams	16
Number of legendre moments	35

Table A2. Spectral bands.

Band	Spectral Range [nm]		
	Start	End	Step
1	757.5	772.7	0.001
2	1594.0	1621.8	0.005
3	2046.5	2082.2	0.005

Table A3. Scattering parameters of scenarios *Baseline*, *SIF*, and XCO_2+6 *ppm*.

Parameter	Band 1	Band 2	Band 3
Albedo	0.20	0.10	0.05
Rayleigh scattering	off	off	off
Aerosols	off	off	off
Clouds	off	off	off

Table A4. Scattering parameters of scenario *Rayleigh*.

Parameter	Band 1	Band 2	Band 3
Albedo	0.20	0.10	0.05
Rayleigh scattering	on	on	on
Aerosols	off	off	off
Clouds	off	off	off

Table A5. Scattering parameters of scenario *Rayleigh+Dark surface*.

Parameter	Band 1	Band 2	Band 3
Albedo	0.14	0.07	0.04
Rayleigh scattering	on	on	on
Aerosols	off	off	off
Clouds	off	off	off

Table A6. Scattering parameters of scenario *Rayleigh+Dark surface*.

Parameter	Band 1	Band 2	Band 3
Albedo	0.14	0.07	0.04
Rayleigh scattering	on	on	on
Aerosols	off	off	off
Clouds	off	off	off

Table A7. Scattering parameters of scenario *Rayleigh+Ocean glint*.

Parameter	Band 1	Band 2	Band 3
Albedo	ocean (wind speed = 5 m/s, 37° relative to the SPP)		
Rayleigh scattering	on	on	on
Aerosol Layer 1			
Top altitude [km]	29.00	29.00	29.00
Aerosol type	background	background	background
Phase Function	Mie	Mie	Mie
Single Scattering Albedo 1	1.000 (694 nm)	0.998 (1536 nm)	0.969 (2000 nm)
Single Scattering Albedo 2	1.000 (860 nm)	0.989 (1800 nm)	0.942 (2250 nm)
Asymmetry Factor 1	0.694 (694 nm)	0.447 (1536 nm)	0.322 (2000 nm)
Asymmetry Factor 2	0.650 (860 nm)	0.372 (1800 nm)	0.269 (2250 nm)

Table A7. *Cont.*

Parameter	Band 1	Band 2	Band 3
Aerosol Layer 2			
Top altitude [km]	10.00	10.00	10.00
Aerosol type	background	background	background
Phase Function	Mie	Mie	Mie
Single Scattering Albedo 1	1.000 (694 nm)	0.998 (1536 nm)	0.969 (2000 nm)
Single Scattering Albedo 2	1.000 (860 nm)	0.989 (1800 nm)	0.942 (2250 nm)
Asymmetry Factor 1	0.694 (694 nm)	0.447 (1536 nm)	0.322 (2000 nm)
Asymmetry Factor 2	0.650 (860 nm)	0.372 (1800 nm)	0.269 (2250 nm)
Aerosol Layer 3			
Top altitude [km]	2.00	2.00	2.00
Aerosol type	background	background	background
Phase Function	Mie	Mie	Mie
Single Scattering Albedo 1	1.000 (694 nm)	0.998 (1536 nm)	0.969 (2000 nm)
Single Scattering Albedo 2	1.000 (860 nm)	0.989 (1800 nm)	0.942 (2250 nm)
Asymmetry Factor 1	0.694 (694 nm)	0.447 (1536 nm)	0.322 (2000 nm)
Asymmetry Factor 2	0.650 (860 nm)	0.372 (1800 nm)	0.269 (2250 nm)
Clouds	off	off	off

Table A8. Scattering parameters of scenario *Rayleigh+Aerosol BG*.

Parameter	Band 1	Band 2	Band 3
Albedo	0.20	0.10	0.05
Rayleigh scattering	on	on	on
Aerosol Layer 1			
Top altitude [km]	29.00	29.00	29.00
Aerosol type	background	background	background
Phase Function	Mie	Mie	Mie
Single Scattering Albedo 1	1.000 (694 nm)	0.998 (1536 nm)	0.969 (2000 nm)
Single Scattering Albedo 2	1.000 (860 nm)	0.989 (1800 nm)	0.942 (2250 nm)
Asymmetry Factor 1	0.694 (694 nm)	0.447 (1536 nm)	0.322 (2000 nm)
Asymmetry Factor 2	0.650 (860 nm)	0.372 (1800 nm)	0.269 (2250 nm)
Aerosol Layer 2			
Top altitude [km]	10.00	10.00	10.00
Aerosol type	background	background	background
Phase Function	Mie	Mie	Mie
Single Scattering Albedo 1	1.000 (694 nm)	0.998 (1536 nm)	0.969 (2000 nm)
Single Scattering Albedo 2	1.000 (860 nm)	0.989 (1800 nm)	0.942 (2250 nm)
Asymmetry Factor 1	0.694 (694 nm)	0.447 (1536 nm)	0.322 (2000 nm)
Asymmetry Factor 2	0.650 (860 nm)	0.372 (1800 nm)	0.269 (2250 nm)
Aerosol Layer 3			
Top altitude [km]	2.00	2.00	2.00
Aerosol type	background	background	background
Phase Function	Mie	Mie	Mie
Single Scattering Albedo 1	1.000 (694 nm)	0.998 (1536 nm)	0.969 (2000 nm)
Single Scattering Albedo 2	1.000 (860 nm)	0.989 (1800 nm)	0.942 (2250 nm)
Asymmetry Factor 1	0.694 (694 nm)	0.447 (1536 nm)	0.322 (2000 nm)
Asymmetry Factor 2	0.650 (860 nm)	0.372 (1800 nm)	0.269 (2250 nm)
Clouds	off	off	off

Table A9. Scattering parameters of scenario *Rayleigh+Aerosol cont.*.

Parameter	Band 1	Band 2	Band 3
Albedo	0.20	0.10	0.05
Rayleigh scattering	on	on	on
Aerosol Layer 1			
Top altitude [km]	29.00	29.00	29.00
Aerosol type	background	background	background
Phase Function	Mie	Mie	Mie
Single Scattering Albedo 1	1.000 (694 nm)	0.998 (1536 nm)	0.969 (2000 nm)
Single Scattering Albedo 2	1.000 (860 nm)	0.989 (1800 nm)	0.942 (2250 nm)
Asymmetry Factor 1	0.694 (694 nm)	0.447 (1536 nm)	0.322 (2000 nm)
Asymmetry Factor 2	0.650 (860 nm)	0.372 (1800 nm)	0.269 (2250 nm)
Aerosol Layer 2			
Top altitude [km]	10.00	10.00	10.00
Aerosol type	continental	continental	continental
Phase Function	Mie	Mie	Mie
Single Scattering Albedo 1	0.884 (694 nm)	0.757 (1536 nm)	0.796 (2000 nm)
Single Scattering Albedo 2	0.847 (860 nm)	0.762 (1800 nm)	0.774 (2250 nm)
Asymmetry Factor 1	0.630 (694 nm)	0.638 (1536 nm)	0.709 (2000 nm)
Asymmetry Factor 2	0.630 (860 nm)	0.672 (1800 nm)	0.731 (2250 nm)
Aerosol Layer 3			
Top altitude [km]	2.00	2.00	2.00
Aerosol type	continental	continental	continental
Phase Function	Mie	Mie	Mie
Single Scattering Albedo 1	0.884 (694 nm)	0.757 (1536 nm)	0.796 (2000 nm)
Single Scattering Albedo 2	0.847 (860 nm)	0.762 (1800 nm)	0.774 (2250 nm)
Asymmetry Factor 1	0.630 (694 nm)	0.638 (1536 nm)	0.709 (2000 nm)
Asymmetry Factor 2	0.630 (860 nm)	0.672 (1800 nm)	0.731 (2250 nm)
Clouds	off	off	off

Table A10. Scattering parameters of scenario *Rayleigh+Aerosol urban*.

Parameter	Band 1	Band 2	Band 3
Albedo	0.20	0.10	0.05
Rayleigh scattering	on	on	on
Aerosol Layer 1			
Top altitude [km]	29.00	29.00	29.00
Aerosol type	background	background	background
Phase Function	Mie	Mie	Mie
Single Scattering Albedo 1	1.000 (694 nm)	0.998 (1536 nm)	0.969 (2000 nm)
Single Scattering Albedo 2	1.000 (860 nm)	0.989 (1800 nm)	0.942 (2250 nm)
Asymmetry Factor 1	0.694 (694 nm)	0.447 (1536 nm)	0.322 (2000 nm)
Asymmetry Factor 2	0.650 (860 nm)	0.372 (1800 nm)	0.269 (2250 nm)
Aerosol Layer 2			
Top altitude [km]	10.00	10.00	10.00
Aerosol type	urban	urban	urban
Phase Function	Mie	Mie	Mie
Single Scattering Albedo 1	0.635 (694 nm)	0.461 (1536 nm)	0.381 (2000 nm)
Single Scattering Albedo 2	0.593 (860 nm)	0.409 (1800 nm)	0.348 (2250 nm)
Asymmetry Factor 1	0.586 (694 nm)	0.566 (1536 nm)	0.584 (2000 nm)
Asymmetry Factor 2	0.584 (860 nm)	0.574 (1800 nm)	0.583 (2250 nm)

Table A10. *Cont.*

Parameter	Band 1	Band 2	Band 3
Aerosol Layer 3			
Top altitude [km]	2.00	2.00	2.00
Aerosol type	urban	urban	urban
Phase Function	Mie	Mie	Mie
Single Scattering Albedo 1	0.635 (694 nm)	0.461 (1536 nm)	0.381 (2000 nm)
Single Scattering Albedo 2	0.593 (860 nm)	0.409 (1800 nm)	0.348 (2250 nm)
Asymmetry Factor 1	0.586 (694 nm)	0.566 (1536 nm)	0.584 (2000 nm)
Asymmetry Factor 2	0.584 (860 nm)	0.574 (1800 nm)	0.583 (2250 nm)
Clouds	off	off	off

Table A11. Scattering parameters of scenario *Rayleigh+Aerosol BG+Water cloud*.

Parameter	Band 1	Band 2	Band 3
Albedo	0.20	0.10	0.05
Rayleigh scattering	on	on	on
Aerosol Layer 1			
Top altitude [km]	29.00	29.00	29.00
Aerosol type	background	background	background
Phase Function	Mie	Mie	Mie
Single Scattering Albedo 1	1.000 (694 nm)	0.998 (1536 nm)	0.969 (2000 nm)
Single Scattering Albedo 2	1.000 (860 nm)	0.989 (1800 nm)	0.942 (2250 nm)
Asymmetry Factor 1	0.694 (694 nm)	0.447 (1536 nm)	0.322 (2000 nm)
Asymmetry Factor 2	0.650 (860 nm)	0.372 (1800 nm)	0.269 (2250 nm)
Aerosol Layer 2			
Top altitude [km]	10.00	10.00	10.00
Aerosol type	background	background	background
Phase Function	Mie	Mie	Mie
Single Scattering Albedo 1	1.000 (694 nm)	0.998 (1536 nm)	0.969 (2000 nm)
Single Scattering Albedo 2	1.000 (860 nm)	0.989 (1800 nm)	0.942 (2250 nm)
Asymmetry Factor 1	0.694 (694 nm)	0.447 (1536 nm)	0.322 (2000 nm)
Asymmetry Factor 2	0.650 (860 nm)	0.372 (1800 nm)	0.269 (2250 nm)
Aerosol Layer 3			
Top altitude [km]	2.00	2.00	2.00
Aerosol type	background	background	background
Phase Function	Mie	Mie	Mie
Single Scattering Albedo 1	1.000 (694 nm)	0.998 (1536 nm)	0.969 (2000 nm)
Single Scattering Albedo 2	1.000 (860 nm)	0.989 (1800 nm)	0.942 (2250 nm)
Asymmetry Factor 1	0.694 (694 nm)	0.447 (1536 nm)	0.322 (2000 nm)
Asymmetry Factor 2	0.650 (860 nm)	0.372 (1800 nm)	0.269 (2250 nm)
Clouds			
Base altitude [km]	3.001	3.001	3.001
Top altitude [km]	2.999	2.999	2.999
Cloud Type	Water	Water	Water
Optical Thickness at 500 nm	0.039	0.039	0.039
LWP [g/m^2]	0.300	0.300	0.300
Phase function	Greek-12	Greek-12	Greek-12

Table A12. Scattering parameters of scenario *Rayleigh+Aerosol BG+Ice cloud*.

Parameter	Band 1	Band 2	Band 3
Albedo	0.20	0.10	0.05
Rayleigh scattering	on	on	on
Aerosol Layer 1			
Top altitude [km]	29.00	29.00	29.00
Aerosol type	background	background	background
Phase Function	Mie	Mie	Mie
Single Scattering Albedo 1	1.000 (694 nm)	0.998 (1536 nm)	0.969 (2000 nm)
Single Scattering Albedo 2	1.000 (860 nm)	0.989 (1800 nm)	0.942 (2250 nm)
Asymmetry Factor 1	0.694 (694 nm)	0.447 (1536 nm)	0.322 (2000 nm)
Asymmetry Factor 2	0.650 (860 nm)	0.372 (1800 nm)	0.269 (2250 nm)
Aerosol Layer 2			
Top altitude [km]	10.00	10.00	10.00
Aerosol type	background	background	background
Phase Function	Mie	Mie	Mie
Single Scattering Albedo 1	1.000 (694 nm)	0.998 (1536 nm)	0.969 (2000 nm)
Single Scattering Albedo 2	1.000 (860 nm)	0.989 (1800 nm)	0.942 (2250 nm)
Asymmetry Factor 1	0.694 (694 nm)	0.447 (1536 nm)	0.322 (2000 nm)
Asymmetry Factor 2	0.650 (860 nm)	0.372 (1800 nm)	0.269 (2250 nm)
Aerosol Layer 3			
Top altitude [km]	2.00	2.00	2.00
Aerosol type	background	background	background
Phase Function	Mie	Mie	Mie
Single Scattering Albedo 1	1.000 (694 nm)	0.998 (1536 nm)	0.969 (2000 nm)
Single Scattering Albedo 2	1.000 (860 nm)	0.989 (1800 nm)	0.942 (2250 nm)
Asymmetry Factor 1	0.694 (694 nm)	0.447 (1536 nm)	0.322 (2000 nm)
Asymmetry Factor 2	0.650 (860 nm)	0.372 (1800 nm)	0.269 (2250 nm)
Clouds			
Base altitude [km]	8.001	8.001	8.001
Top altitude [km]	7.999	7.999	7.999
Cloud Type	Ice	Ice	Ice
Optical Thickness at 500 nm	0.033	0.033	0.033
IWP [g/m^2]	1.000	1.000	1.000
Phase function	Greek_Fractal_50	Greek_Fractal_50	Greek_Fractal_50

References

1. Reuter, M.; Buchwitz, M.; Hilker, M.; Heymann, J.; Bovensmann, H.; Burrows, J.P.; Houweling, S.; Liu, Y.Y.; Nassar, R.; Chevallier, F.; et al. How Much CO_2 Is Taken Up by the European Terrestrial Biosphere? *Bull. Am. Meteorol. Soc.* **2017**, *98*, 665–671.
2. Miller, C.E.; Crisp, D.; DeCola, P.L.; Olsen, S.C.; Randerson, J.T.; Michalak, A.M.; Alkhaled, A.; Rayner, P.; Jacob, D.J.; Suntharalingam, P.; et al. Precision requirements for space-based X_{CO_2} data. *J. Geophys. Res.* **2007**, *112*, doi:10.1029/2006JD007659.
3. Chevallier, F.; Bréon, F.M.; Rayner, P.J. Contribution of the Orbiting Carbon Observatory to the estimation of CO_2 sources and sinks: Theoretical study in a variational data assimilation framework. *J. Geophys. Res.* **2007**, *112*, doi:10.1029/2006JD007375.
4. Bovensmann, H.; Buchwitz, M.; Burrows, J.P.; Reuter, M.; Krings, T.; Gerilowski, K.; Schneising, O.; Heymann, J.; Tretner, A.; Erzinger, J. A remote sensing technique for global monitoring of power plant CO_2 emissions from space and related applications. *Atmos. Meas. Tech.* **2010**, *3*, 781–811.
5. Houweling, S.; Hartmann, W.; Aben, I.; Schrijver, H.; Skidmore, J.; Roelofs, G.J.; Breon, F.M. Evidence of systematic errors in SCIAMACHY-observed CO_2 due to aerosols. *Atmos. Chem. Phys.* **2005**, *5*, 3003–3013.

6. Aben, I.; Hasekamp, O.; Hartmann, W. Uncertainties in the space-based measurements of CO_2 columns due to scattering in the Earth's atmosphere. *J. Quant. Spectrosc. Radiat. Transf.* **2007**, *104*, 450–459.
7. Schneising, O.; Buchwitz, M.; Burrows, J.P.; Bovensmann, H.; Reuter, M.; Notholt, J.; Macatangay, R.; Warneke, T. Three years of greenhouse gas column-averaged dry air mole fractions retrieved from satellite—Part 1: Carbon dioxide. *Atmos. Chem. Phys.* **2008**, *8*, 3827–3853.
8. Reuter, M.; Buchwitz, M.; Schneising, O.; Heymann, J.; Bovensmann, H.; Burrows, J.P. A method for improved SCIAMACHY CO_2 retrieval in the presence of optically thin clouds. *Atmos. Meas. Tech.* **2010**, *3*, 209–232.
9. Butz, A.; Guerlet, S.; Hasekamp, O.; Schepers, D.; Galli, A.; Aben, I.; Frankenberg, C.; Hartmann, J.M.; Tran, H.; Kuze, A.; et al. Toward accurate CO_2 and CH_4 observations from GOSAT. *Geophys. Res. Lett.* **2011**, *38*, doi:10.1029/2011GL047888.
10. Cogan, A.J.; Boesch, H.; Parker, R.J.; Feng, L.; Palmer, P.I.; Blavier, J.F.L.; Deutscher, N.M.; Macatangay, R.; Notholt, J.; Roehl, C.; et al. Atmospheric carbon dioxide retrieved from the Greenhouse gases Observing SATellite (GOSAT): Comparison with ground-based TCCON observations and GEOS-Chem model calculations. *J. Geophys. Res. Atmos.* **2012**, *117*, doi:10.1029/2012JD018087.
11. Yoshida, Y.; Kikuchi, N.; Morino, I.; Uchino, O.; Oshchepkov, S.; Bril, A.; Saeki, T.; Schutgens, N.; Toon, G.C.; Wunch, D.; et al. Improvement of the retrieval algorithm for GOSAT SWIR XCO_2 and XCH_4 and their validation using TCCON data. *Atmos. Meas. Tech.* **2013**, *6*, 1533–1547.
12. O'Dell, C.W.; Connor, B.; Bösch, H.; O'Brien, D.; Frankenberg, C.; Castano, R.; Christi, M.; Eldering, D.; Fisher, B.; Gunson, M.; et al. The ACOS CO_2 retrieval algorithm - Part 1: Description and validation against synthetic observations. *Atmos. Meas. Tech.* **2012**, *5*, 99–121.
13. Timofeyev, Y.M.; Vasilyev, A.; Rozanov, V. Information content of the spectral measurements of the 0.76 μm O2 outgoing radiation with respect to the vertical aerosol optical properties. *Adv. Space Res.* **1995**, *16*, 91–94.
14. Schuessler, O.; Rodriguez, D.G.L.; Doicu, A.; Spurr, R. Information Content in the Oxygen *A*-Band for the Retrieval of Macrophysical Cloud Parameters. *IEEE Trans. Geosci. Remote Sens.* **2014**, *52*, 3246–3255.
15. Colosimo, S.F.; Natraj, V.; Sander, S.P.; Stutz, J. A sensitivity study on the retrieval of aerosol vertical profiles using the oxygen A-band. *Atmos. Meas. Tech.* **2016**, *9*, 1889–1905.
16. Buchwitz, M.; Rozanov, V.V.; Burrows, J.P. A correlated-k distribution scheme for overlapping gases suitable for retrieval of atmospheric constituents from moderate resolution radiance measurements in the visible/near-infrared spectral region. *J. Geophys. Res.* **2000**, *105*, 15247–15261.
17. Reuter, M.; Thomas, W.; Albert, P.; Lockhoff, M.; Weber, R.; Karlsson, K.G.; Fischer, J. The CM-SAF and FUB cloud detection schemes for SEVIRI: Validation with synoptic data and initial comparison with MODIS and CALIPSO. *J. Appl. Meteorol. Climatol.* **2009**, *48*, 301–316.
18. Schneising, O.; Bergamaschi, P.; Bovensmann, H.; Buchwitz, M.; Burrows, J.P.; Deutscher, N.M.; Griffith, D.W.T.; Heymann, J.; Macatangay, R.; Messerschmidt, J.; et al. Atmospheric greenhouse gases retrieved from SCIAMACHY: Comparison to ground-based FTS measurements and model results. *Atmos. Chem. Phys.* **2012**, *12*, 1527–1540.
19. Bril, A.; Oshchepkov, S.; Yokota, T.; Inoue, G. Parameterization of aerosol and cirrus cloud effects on reflected sunlight spectra measured from space: Application of the equivalence theorem. *Appl. Opt.* **2007**, *46*, 2460–2470.
20. Bril, A.; Oshchepkov, S.; Yokota, T. Application of a probability density function-based atmospheric light-scattering correction to carbon dioxide retrievals from GOSAT over-sea observations. *Remote Sens. Environ.* **2012**, *117*, 301–306.
21. Crisp, D.; Atlas, R.M.; Bréon, F.M.; Brown, L.R.; Burrows, J.P.; Ciais, P.; Connor, B.J.; Doney, S.C.; Fung, I.Y.; Jacob, D.J.; et al. The Orbiting Carbon Observatory (OCO) mission. *Adv. Space Res.* **2004**, *34*, 700–709.
22. Crisp, D.; Pollock, H.R.; Rosenberg, R.; Chapsky, L.; Lee, R.A.M.; Oyafuso, F.A.; Frankenberg, C.; O'Dell, C.W.; Bruegge, C.J.; Doran, G.B.; et al. The on-orbit performance of the Orbiting Carbon Observatory-2 (OCO-2) instrument and its radiometrically calibrated products. *Atmos. Meas. Tech.* **2017**, *10*, 59–81.
23. Kuze, A.; Suto, H.; Nakajima, M.; Hamazaki, T. Thermal and near infrared sensor for carbon observation Fourier-transform spectrometer on the Greenhouse Gases Observing Satellite for greenhouse gases monitoring. *Appl. Opt.* **2009**, *48*, doi:10.1364/AO.48.006716.
24. Nelson, R.R.; O'Dell, C.W.; Taylor, T.E.; Mandrake, L.; Smyth, M. The potential of clear-sky carbon dioxide satellite retrievals. *Atmos. Meas. Tech.* **2016**, *9*, 1671–1684.

25. Reuter, M.; Buchwitz, M.; Schneising, O.; Noël, S.; Bovensmann, H.; Burrows, J.P. A fast atmospheric trace gas retrieval for hyperspectral instruments approximating multiple scattering—Part 2: Application to XCO_2 retrievals from OCO-2. *Remote Sens.* **2017**, *9*, doi:10.3390/rs9111102.
26. Roedel, W.; Wagner, T. *Physik unserer Umwelt: Die Atmosphäre*; Springer: Berlin/Heidelberg, Germany, 2011.
27. Bennartz, R.; Preusker, R. Representation of the photon pathlength distribution in a cloudy atmosphere using finite elements. *J. Quant. Spectrosc. Radiat. Transf.* **2006**, *98*, 202–219.
28. Rodgers, C.D. *Inverse Methods for Atmospheric Sounding: Theory and Practice*; World Scientific Publishing: Singapore, Singapore, 2000.
29. Frankenberg, C.; Butz, A.; Toon, G.C. Disentangling chlorophyll fluorescence from atmospheric scattering effects in O2 A-band spectra of reflected sun-light. *Geophys. Res. Lett.* **2011**, *38*, doi:10.1029/2010GL045896.
30. Reuter, M.; Buchwitz, M.; Schneising, O.; Hase, F.; Heymann, J.; Guerlet, S.; Cogan, A.J.; Bovensmann, H.; Burrows, J.P. A simple empirical model estimating atmospheric CO_2 background concentrations. *Atmos. Meas. Tech.* **2012**, *5*, 1349–1357.
31. Peters, W.; Jacobson, A.R.; Sweeney, C.; Andrews, A.E.; Conway, T.J.; Masarie, K.; Miller, J.B.; Bruhwiler, L.M.P.; Petron, G.; Hirsch, A.I.; et al. An atmospheric perspective on North American carbon dioxide exchange: CarbonTracker. *Proc. Natl. Acad. Sci. USA* **2007**, *104*, 18925–18930.
32. Thompson, D.R.; Chris Benner, D.; Brown, L.R.; Crisp, D.; Malathy Devi, V.; Jiang, Y.; Natraj, V.; Oyafuso, F.; Sung, K.; Wunch, D.; et al. Atmospheric validation of high accuracy CO_2 absorption coefficients for the OCO-2 mission. *J. Quant. Spectrosc. Radiat. Transf.* **2012**, *113*, 2265–2276.
33. Kurucz, H.L. The Solar Spectrum: Atlases and Line Identifications, Workshop on Laboratory and Astronomical High Resolution Spectra. Astronomical Society of the Pacific Conference Series. In Proceedings of the ASP Conference, Brussels, Belgium, 29 August–2 September 1994; pp. 17–31.
34. Rascher, U.; Agati, G.; Alonso, L.; Cecchi, G.; Champagne, S.; Colombo, R.; Damm, A.; Daumard, F.; de Miguel, E.; Fernandez, G.; et al. CEFLES2: The remote sensing component to quantify photosynthetic efficiency from the leaf to the region by measuring sun-induced fluorescence in the oxygen absorption bands. *Biogeosciences* **2009**, *6*, 1181–1198.
35. Rozanov, V.; Rozanov, A.; Kokhanovsky, A.; Burrows, J. Radiative transfer through terrestrial atmosphere and ocean: Software package SCIATRAN. *J. Quant. Spectrosc. Radiat. Transf.* **2014**, *133*, 13–71.
36. Buchwitz, M.; Reuter, M.; Bovensmann, H.; Pillai, D.; Heymann, J.; Schneising, O.; Rozanov, V.; Krings, T.; Burrows, J.P.; Boesch, H.; et al. Carbon Monitoring Satellite (CarbonSat): assessment of atmospheric CO_2 and CH_4 retrieval errors by error parameterization. *Atmos. Meas. Tech.* **2013**, *6*, 3477–3500.